Centro de Investigación Científica y de Educación Superior de Ensenada, Baja California

Maestría en Ciencias

en Ciencias de la Tierra con orientación en Sismología

Numerical solution of the Green's function for anisotropic solids using the Radon transform

Tesis

para cubrir parcialmente los requisitos necesarios para obtener el grado de

Maestro en Ciencias

Presenta:

Gerardo Agustín López Martínez

Ensenada, Baja California, México

2019

Tesis defendida por

Gerardo Agustín López Martínez

y aprobada por el siguiente Comité

Dr. Pratap Narayan Sahay Sahay

Director del Comité

Dr. Jonás de Dios De Basabe Delgado

Dr. Markus Sebastian Gross

Dr. Jonás de Dios De Basabe Delgado

Coordinador del Programa de Posgrado en Ciencias de la Tierra

---

Dra. Rufina Hernández Martínez

Directora de Estudios de Posgrado

Gerardo Agustín López Martínez © 2019
Queda prohibida la reproducción parcial o total de esta obra sin el permiso formal y explícito del autor

Resumen de la tesis que presenta Gerardo Agustín López Martínez como requisito parcial para la obtención del grado de Maestro en Ciencias en Ciencias de la Tierra con orientación en Sismología.

Solución numérica de la función de Green para sólidos anisotrópicos usando la transformada de Radón

Resumen aprobado por:

Dr. Pratap Narayan Sahay Sahay
Director de tesis

El estudio de la anisotropía es de vital importancia porque las formaciones geológicas encontradas en la exploración de hidrocarburos son usualmente medios estratificados o fracturados. Para esto, la solución de una función de Green es de interés porque puede ser usada para la construcción de soluciones más generales. El propósito de este estudio es la implementación numérica de la solución para la función anisotrópica de Green usando la transformada de Radón en un medio elástico. En esta metodología, aplicando la transformada de Radón, las ecuaciones que rigen el sistema de ecuaciones diferenciales parciales se reduce a un sistema de ecuaciones diferenciales ordinarias, el cual se desacopla utilizando los eigenvalores y eigenvectores de dicho sistema. Para regresar al dominio inicial, la transformada inversa de Radón se define como una integral sobre una esfera cerrada que se calcula numéricamente sin complicaciones utilizando la cuadratura gaussiana para todo tipo de simetrías. Los resultados del calculo numérico de esta solución se presenta para los casos de anisotropía transversalmente isotrópica, ortorrómbica y monoclínica. Además, se muestra el estudio de la variación de la forma de onda respecto al angulo polar para el caso transversalmente isotrópico. Los resultados nos muestran que mediante esta metodología se puede estudiar la forma de onda, la separación de las ondas S y la dependencia angular del movimiento de partícula para medios anisotrópicos de una forma eficiente.

Palabras Clave: **Anisotropía, Función de Green, Transformada de Radón, Propagación de ondas**

Abstract of the thesis presented by Gerardo Agustín López Martínez as a partial requirement to obtain the Master of Science degree in Master in Earth Science with orientation in Seismology.

Numerical solution of the Green's function for anisotropic solids using the Radon transform

Abstract approved by:

Dr. Pratap Narayan Sahay Sahay
Thesis Director

The study of anisotropy is vital because geological formations encountered in hydrocarbon exploration are usually stratified or fractured. For this, the solution of a Green's function is of interest since it can be used for constructing more general solutions. The purpose of this study is the numerical implementation of the solution of the anisotropic elastic Green's function using the Radon transform approach. In this approach, by applying the Radon transform, the governing system of a partial differential equation reduces to a system of ordinary differential equations, which is then decoupled using the eigenvalues and eigenvectors of that system. To return to the spatial domain the inverse Radon transform is used, which is a double integral over the unit-sphere that is calculated numerically using Gaussian quadrature without complications for all classes of symmetries. The results of the numerical calculation of this solution are presented for cases of transversely isotropic, orthorhombic, and monoclinic anisotropy. Also presented is a study of the variation of waveform with respect to polar angle for the transversely isotropic case. These results show that through this methodology, the waveform, the separation of the S-wave, and the angular dependence of the particle movement can be studied efficiently.

Keywords: **Anisotropy, Green's function, Radon transform, Wave propagation**

Dedicatoria

A Dios, mis padres y familia.

Agradecimientos

Principalmente a Dios por todas sus bendiciones, por guiarme a lo largo de nuestra existencia, ser el apoyo y fortaleza en aquellos momentos de dificultad y de debilidad.

Al Centro de Investigación Científica y de Educación Superior de Ensenada (CICESE) por permitirme esta oportunidad de desarrollo personal.

Al Consejo Nacional de Ciencia y Tecnología (CONACyT) por brindarme el apoyo económico para la realización de este proyecto como becario No.639314.

Al Dr. Pratap Sahay por su constante apoyo, consejos y atención, a mis sinodales el Dr. Jonás D. de Basabe y Dr. Markus Gross por su tiempo y observaciones para la mejora de mi trabajo.

A mis padres, Agustin y Julieta, por ser mi pilar fundamental y haberme apoyado incondicionalmente, pese a las adversidades e inconvenientes que se presentaron.

A mis hermanas, Ivette y Melissa, por sus constantes llamadas de ánimo y consejos.

A mi novia Marilu por la ayuda brindada, por estar a mi lado en los momentos y situaciones dificiles. Me ayudaste hasta donte te era posible e incluso más que eso.

Al equipo de trabajo del laboratorio, Marco, Josue, Gabriel, Anita, por su constante ayuda y consejos durante todo mi trabajo de tesis.

A mis compañeros del posgrado, Eleyra, Jorge, Angel, Young, Roberto, Raul, Liza, Arisai, Halia, y demás que compartieron conmigo tanto buenos, como malos momentos.

Al personal administrativo de CICESE, por su atención y orientación.

Contents

Page

Abstract in Spanish ii

Abstract in English iii

Dedication iv

Acknowledgements v

List of figures viii

List of tables ix

Chapter 1 Introduction 1

1.1 Hyphotesis 2

1.2 Thesis objectives 2

1.3 Outline of the thesis 3

Chapter 2 Equation of motion for anisotropic solids 4

2.1 Foundations of linear elastodynamics 4

2.2 Elastic stiffness tensor 7

2.3 Elastic anisotropy of geological rocks 10

2.3.1 Monoclinic symmetry 11

2.3.2 Orthorhombic symmetry 11

2.3.3 Transversely isotropic symmetry 12

2.4 Green's function in the $\mathbf{k}$ and ω domain 14

Chapter 3 Closed-form solution for the anisotropic Green's function 17

3.1 The Radon transform 17

3.1.1 Preliminaries 17

3.1.2 Integration over unit sphere 18

3.1.3 Some properties of Radon transform 19

3.2 Solution of 3-D Helmholtz equation using the Radon transform 20

3.3 Radon transform approach for the anisotropic Green's function 22

3.3.1 Numerical integration by Gaussian quadrature method 25

Chapter 4 Numerical solution for the anisotropic Green's function 29

4.1 Validation with the analytical solution in isotropic medium 29

4.2 Validation with pure direction velocities in transversely isotropic medium 31
4.3 Numerical solution for the anisotropic Green's function in VTI symmetry 34
4.4 Numerical solution for the anisotropic Green's function in orthorhombic symmetry 35
4.5 Numerical solution for the anisotropic Green's function in monoclinic symmetry 36
4.6 Point-source radiation pattern: Transversely isotropic case 38

Chapter 5 Concluding remarks and future work directions 43

Cited literature 45

Appendix A Phase velocities in an arbitrary anisotropic medium 46

List of figures

Figure — Page

1 Cartoon of a layered medium permeated by a tilted set of fractures that exhibits monoclinic anisotropy. . . . 11

2 Cartoon of layered medium permeated by orthogonal set of fractures to the lamination that exhibits orthorhombic anisotropy. . . . 12

3 Cartoons of layered media that exhibit transversely isotropic anisotropy. VTI (left), HTI (center) and TTI (right). . . . 13

4 (Left) Illustration of vectors $\mathbf{x}, \mathbf{e}, \mathbf{d}$ and $\mathbf{n}$ in the fixed x_i coordinates. (Right) Relation between these vectors on the unit circle. . . . 18

5 Numerical integration. (a) Exact integral. (b) Approximate integral. (Adopted from Hoffman (1992)). . . . 26

6 Comparison between analytical solution and numerical solution in isotropic medium. 30

7 Scaled displacement (by c_{44} parameter) measured in pure direction of VTI symmetry. The geophones are located in 400m., 700m., 1000m. and 1300m. Source is a Ricker pulse of amplitude 1. . . . 31

8 Scaled displacement (by c_{44} parameter) measured in pure direction of HTI symmetry. The geophones are located in 400m., 700m., 1000m. and 1300m. Source is a Ricker pulse of amplitude 1. . . . 32

9 G_{11}, G_{22} and G_{33} solutions for VTI symmetry. The color marks correspond to the travel time of the first arrival of the wavefields. . . . 34

10 G_{11}, G_{22} and G_{33} solutions for orthorhombic symmetry. The color marks correspond to the travel time of the first arrival of the wavefields. . . . 36

11 G_{11}, G_{22} and G_{33} solutions for monoclinic symmetry. The color marks correspond to the travel time of the first arrival of the wavefields. . . . 37

12 Radiation pattern of qP-wave in G_{11} component. The wave amplitude is normalized by 1. The color mark corresponds to the travel time of the first arrival of the wavefield. 38

13 Radiation pattern of qP-wave in G_{22} component. The wave amplitude is normalized by 1. The color mark corresponds to the travel time of the first arrival of the wavefield. 39

14 Radiation pattern of qP-wave in G_{33} component. The wave amplitude is normalized by 1. The color mark corresponds to the travel time of the first arrival of the wavefield. 39

15 Radiation pattern of qSV- and qSH-waves in G_{11} component. The wave amplitude is normalized by 1. The color marks corresponds to the travel time of the first arrival of the wavefields. . . . 40

16 Radiation pattern of qSV- and qSH-waves in G_{22} component. The wave amplitude is normalized by 1. The color marks corresponds to the travel time of the first arrival of the wavefields. . . . 40

17 Radiation pattern of qSV- and qSH-waves in G_{33} component. The wave amplitude is normalized by 1. The color marks corresponds to the travel time of the first arrival of the wavefields. . . . 41

List of tables

Table		Page
1	Relation between the number of elastic constants and symmetries.	10
2	Gaussian quadrature parameters.	27
3	List of parameters for isotropic case. r_0 corresponds to the distance between source and receiver.	29
4	Comparison of velocities for isotropic case.	30
5	List of parameters for transversely isotropic case. This parameters correspond to a cubic ice with hexagonal symmetry. r_0, Δr and $\# \, geophones$ are, respectively, the distance between source and first receiver, the increment of distance between each receiver, and the number of geophones.	31
6	Comparison of velocities for VTI medium.	33
7	Comparison of velocities for HTI medium.	33
8	List of parameters for VTI symmetry. The elastic constants correspond to a Cretaceous shale taken from Ikelle & Amundsen (2018).	34
9	List of parameters for orthorhombic symmetry. The elastic constants are taken from Ikelle & Amundsen (2018).	35
10	List of parameters for monoclinic symmetry. The elastic constants are taken from Nevitt *et al.* (1988).	37

Chapter 1 Introduction

Geological formations encountered in hydrocarbon exploration are usually layered and fractured, due to diverse processes such as deposition of sediments and tectonic forces. For a seismic wave, a finely layered rock appears as transversely isotropic. A finely layered medium permeated by fractures orthogonal to lamination manifests itself as orthorhombic, and for a tilted set of fractures, it is monoclinic. In such settings, shear wave splitting, directional dependence of waves velocities and tilting away of particle motion occur, which are the expression of seismic anisotropy (Crampin, 1985; Helbig, 1994). There has been much interest in the exploration of unconventional resources in the past decades. These are geological formations that have very low permeability or high viscosity such as tight-gas sandstone, shale gas, coalbed methane, shale oil or tar sands, heavy oil and gas hydrates. These rocks invariably exhibit seismic anisotropy (Zee Ma & Holditch, 2016). Therefore, the study of elastic waves in anisotropic solids is of importance in reservoir seismology.

The development of the foundations of anisotropic elasticity traces back to the 19th century, and the principal contributors were G. R. Hamilton, G. Green, W. Thomsen (Lord Kelvin) and E.B. Christoffel (Helbig, 2003). Rudzki (1898) introduced anisotropic elasticity to model waves in rocks. There is a vast literature on waves in anisotropic solids, which mostly deals with plane-wave solutions for different classes of anisotropic symmetries. An excellent review of such problems is presented in the book of Auld (1973), and the understanding of seismic anisotropy in reservoirs in Thomsen (2002). However, full-wave solutions for anisotropic solids is still far from complete.

The study of anisotropic models, by a fundamental singular solution, is of interest because it is a basic building block for the construction of more general solutions. The Fourier transform method is the usual approach to construct such a solution. Here, the solution is at first built in the wavenumber-frequency domain and then transformed back to space-time domain. This inverse transformation involves infinite integrals over wavenumbers and frequency, which are tedious to evaluate because the integration kernel has singularities and branch cuts. Early applications to general anisotropy have focused mainly on asymptotic solutions in the far-field. These contributions are reviewed by Kraut (1963), Musgrave (1970), and Payton (1983). For the case of transversely isotropic symmetry, Ben-Menahem and Sena (1990), extending the approach of Buchwald (1959), obtained a solution in a closed-form which was further simplified by Dong & Schmitt (1994) to make it numerically computable. However, for other classes of anisotropy, numerically comput-

ing the Green's function using the Fourier transform method remains a challenge.

Wang & Achenbach (1995) developed the displacement Green's function by applying the Radon transform in the spatial domain in conjunction with the temporal Fourier transform, which is valid for all classes of anisotropy. In this approach, by applying the Radon transform, the governing system of PDEs reduces to a system of ODEs, which is then decoupled using the eigenvalues and eigenvectors of that system. The solution of decoupled ODEs, in the Radon domain, is straight forward. The inverse Radon transformation, which takes the solution back to the spatial domain, is an integral over a unit sphere. This solution in terms of integral over unit sphere traces back to the works of Burridge (1967) and Willis (1980). Since this closed-form analytic solution is a finite integral, the numerical evaluation can be made efficiently.

The subject matter of this thesis is the numerical implementation of the displacement Green's function for all classes of anisotropic solids obtained by using the Radon transform and compute synthetic seismograms generated by a point source.

1.1 Hyphotesis

The numerical solution of displacement Green's function for an anisotropic elastic solid can be computed easily using the Radon transform approach since the closed-form solution herein is a double integral over a finite domain.

1.2 Thesis objectives

The objective of this work is to develop a numerical solution for the anisotropic Green's function based on the closed-form solution obtained by the Radon transform approach. To accomplish this, the following are the specific objectives:

1. Develop a Gaussian quadrature integration code to compute the numerical solution for the anisotropic Green's function in elastodynamics based on the Radon transform approach by Wang & Achenbach (1995).

2. Validate the numerical solution in the isotropic limit.

3. Validate the solution with pure wave velocities in transversely isotropic case.

4. Compute synthetic seismograms generated by a point source for transversely isotropic, orthorhombic, and monoclinic symmetries.

1.3 Outline of the thesis

An overview of the elastodynamics wave equation is presented in Chapter 2, with details of the development of this governing equation, the inclusion of anisotropy, the relation of this anisotropy with geological rocks, and how the construction of the anisotropic Green's function using the Fourier transform approach becomes tedious. The Radon transform approach to solve a partial differential equation is presented, in Chapter 3, followed by an illustration of this methodology, the development of the analytic solution of anisotropic Green's function using the Radon transform, and the procedure for the numerical evaluation of the analytic solution. The solution is in a closed-form, expressed as finite integrals, which are evaluated numerically using the Gaussian quadrature method. The validation of the numerical solution and computation of wave fields for anisotropic cases are presented in Chapter 4. The validation is accomplish by comparing with the exact solution for isotropic case, and the pure directions velocities for anisotropic cases. The computed wave fields are for vertical transverse isotropy, horizontal transverse isotropy, orthorhombic and monoclinic symmetries. They show shear wave splitting, directional dependence of waves velocities and tilt in polarizations. The concluding remarks and future work directions are presented in Chapter 5.

Chapter 2 Equation of motion for anisotropic solids

The foundations of the governing equations for linear elastodynamics, symmetries of the stiffness tensor and a description of anisotropy in rocks encountered in hydrocarbon exploration are presented in this chapter. A brief description of the governing equations of linear elastodynamics is in §2.1. Anisotropy in elasticity theory emanates from the stiffness tensor of the constitutive equation. The specific forms of stiffness tensor relevant for seismic anisotropy are in §2.2. §2.3 shows how stratification and fractures in rocks relate to seismic anisotropy. Finally, in §2.4, the Green's function is constructed in wavenumber-frequency domain by Fourier transform approach. The solution in space-time domain is obtained by applying the inverse Fourier transformation. As will be shown, only for the case of isotropy, one can evaluate this inverse transformation explicitly. For anisotropy cases, it is a tedious task since it involves infinite integrals over a kernel that has singularities and branch cuts.

2.1 Foundations of linear elastodynamics

Elasticity theory is a mathematical framework which describes mechanical deformation of materials on a continuum scale. The continuous distribution of mass is fundamental to this framework. Here, each material point is assigned with a mass density, ρ. The other two thermodynamic quantities pertaining to the motion of a material point are the velocity field, v_i, and the stress field, σ_{jk}[1].
The velocity field, v_i, associated with a material point is defined by the continuity equation, i.e., the conservation of mass equation

$$\frac{\partial \rho}{\partial t} + \frac{\partial}{\partial x_i}\left(\rho v_i\right) = 0. \tag{1}$$

Clearly, $\mathbf{v}$ is the velocity vector with which mass of the continuum is conserved. The term $\rho\mathbf{v}$ is the mass flux density, which is the linear momentum (per unit volume) of the continuum, and it defines the direction of motion of the material point. The conservation of linear momentum is described by

$$\frac{\partial}{\partial t}(\rho v_i) = \frac{\partial \sigma_{ij}}{\partial x_j} \tag{2}$$

[1]Latin indices $i, j, k...$ and so on run over three spatial coordinate labels, taken as 1,2,3. Subscript $i, j, k...$ indicates a spatial component. Repeated indices indicate summation.

that prescribes the stress field, σ_{ij}, which is associated with the deformation force within a material point. The left and right-hand sides of the above equation are, respectively, inertial and deformational forces. Therefore, it is the statement of Newton's second law of motion for continuum matter. However, this system is not complete because it is a set of three equations with nine variables, namely, three components of the velocity field (v_i) and six components from the stress tensor (σ_{jk}). [2]

To complete this system of equations, based on the first law of Thermodynamics, through the concept of deformational energy potential, the stress tensor is introduced as

$$\sigma_{ij} = c_{ijkl}\ e_{kl}, \tag{3}$$

which is a set of six independent equations, however, it also introduces additional six variables on account of the strain field, e_{kl}. Here c_{ijkl} is a fourth rank tensor known as the elastic stiffness tensor, and the strain field is a second rank symmetric tensor, which is taken as the complete measure of deformation in elasticity theory. For the framework of linear elasticity theory, the deformational energy potential (W) is taken as the quadratic function of the strain field,

$$W = c_{ijkl}\ e_{ij}\ e_{kl}. \tag{4}$$

The gradient of the deformational energy potential with respect to the strain field is the definition of stress field

$$\sigma_{ij} = \frac{\partial W}{\partial e_{ij}}. \tag{5}$$

The definitions 4 and 5 underpin the constitutive equation 3. Although 3 is a set of nine equations, because of the symmetries of stress and strain tensors, three of them are redundant. Likewise, the symmetries of the stress and strain tensors, the elastic stiffness tensor has pairwise symmetry,

$$c_{ijkl} = c_{jikl} = c_{ijlk}, \tag{6}$$

and on account of the existence of the energy potential (4), it also has pair exchange symmetry,

$$c_{ijkl} = c_{klij}. \tag{7}$$

[2] The stress field is a second rank tensor, so it has nine components. Yet only six of those are independent, as it is symmetric since the existence of the intrinsic rotation is ruled out in the elasticity theory.

These symmetries reduce the number of independent coefficients of the fourth rank elastic stiffness tensor from 81 to 21.

Through the definition of the strain tensor, which is the symmetrical part of the deformation gradient tensor $\left(\frac{\partial u_k}{\partial x_l}\right)$, an additional six equations are introduced as

$$e_{kl} = \frac{1}{2}\left(\frac{\partial u_k}{\partial x_l} + \frac{\partial u_l}{\partial x_k}\right). \tag{8}$$

Thus, from equations (2) , (3) and (8), there are fifteen governing equations with eighteen variables, namely, three components of the velocity field (v_i), six components of stress field (σ_{ij}), six components of the strain field (e_{ij}) and three components of displacement field (u_j).

The closure to the system of equations is provided by linking the displacement and velocity fields of the mass particle which rise to three additional equations. This link is stated as

$$v_j\left(\delta_{ij} - \frac{\partial u_i}{\partial x_j}\right) = \frac{\partial u_i}{\partial t}, \tag{9}$$

and to the first order approximation, which is valid for a linear wave propagation problem, it is

$$v_i = \frac{\partial u_i}{\partial t}. \tag{10}$$

Substituting equations (3), (8) and (10) into equation (2), the governing equation of motion, in terms of the displacement field, is obtained as a set of 3x3 coupled second order partial differential equation

$$\left(\delta_{ik}\,\rho\frac{\partial^2}{\partial t^2} - \frac{\partial}{\partial x_j}c_{ijkl}\frac{\partial}{\partial x_l}\right)u_k = 0. \tag{11}$$

When this wave operator is invariant under any rotation with respect to all three coordinate axes, it is regarded as isotropic; otherwise, it is anisotropic.

In an isotropic medium, the solution of the equation of motion in the displacement field supports two different waves, the P-wave and S-wave. The first one, also called compressional wave, travels along the propagation direction. The S-wave, also called transverse wave, has particle motion perpendicular to the direction of propagation. It is a combination of two motions that are orthogonal to each other as well the direction of propagation, and they propagate with the same speed, hence,

combine into single shear motion.

For an anisotropic medium, the two shear motion are no longer propagating with the same speed. This phenomenon is known as shear wave splitting. Thus, in an anisotropic medium, there are three distinct waves. Furthermore, the velocities of these waves are direction-dependent. Moreover, the particle motion associated with the waves is no longer perfectly aligned to the direction propagation or orthonormal to the direction of propagation. Because of that, they are labeled: qP-, qS_1- and qS_2-waves. The meaning of prefix q (quasi) is that particle motion does not have a pure longitudinal or pure transverse polarization direction.
The study of a fundamental solution for the above, i.e., the Green's function, is the subject matter of this work. The equation for Green's function takes the form

$$\left[\delta_{ik}\,\rho\frac{\partial^2}{\partial t^2}-\frac{\partial}{\partial x_j}c_{ijkl}\frac{\partial}{\partial x_l}\right]G_{km}\left(\mathbf{x}-\mathbf{x}';t-t'\right)=-\delta_{im}\delta\left(\mathbf{x}-\mathbf{x}'\right)\delta\left(t-t'\right). \tag{12}$$

The structure of the elastic stiffness tensor is explored in the next section.

2.2 Elastic stiffness tensor

Elastic stiffness tensor describes how an object resists deformation in response to an applied force. To understand its transformation under rotation, the redundancy in the constitutive equation, arising due to the symmetries of the stress and strain tensor, is eliminated by casting the constitutive equation in a 6x6 matrix form. This is achieved by introducing Voigt notation. In this notation, each pair of indices $ij(kl)$ are replaced by one index $I(J)$ using the convention $11, 22, 33, 23, 31, 12 \leftrightarrow 1, 2, 3, 4, 5, 6$. Therefore, in this notation, stress and strain tensors are represented by a six-element column vector rather than a nine-element square matrices

$$\begin{bmatrix}\sigma_{11} &= &\sigma_1\\ \sigma_{22} &= &\sigma_2\\ \sigma_{33} &= &\sigma_3\\ \sigma_{23} &= &\sigma_4\\ \sigma_{13} &= &\sigma_5\\ \sigma_{12} &= &\sigma_6\end{bmatrix}\quad,\quad\begin{bmatrix}e_{11} &= &e_1\\ e_{22} &= &e_2\\ e_{33} &= &e_3\\ 2e_{23} &= &e_4\\ 2e_{13} &= &e_5\\ 2e_{12} &= &e_6\end{bmatrix} \tag{13}$$

and the elastic stiffness tensor c_{ijkl} is a 6x6 symmetric matrix

$$c_{IJ} = \begin{bmatrix} c_{11} & c_{12} & c_{13} & c_{14} & c_{15} & c_{16} \\ c_{12} & c_{22} & c_{23} & c_{24} & c_{25} & c_{26} \\ c_{13} & c_{23} & c_{33} & c_{34} & c_{35} & c_{36} \\ c_{14} & c_{24} & c_{34} & c_{44} & c_{45} & c_{46} \\ c_{15} & c_{25} & c_{35} & c_{45} & c_{55} & c_{56} \\ c_{16} & c_{26} & c_{36} & c_{46} & c_{56} & c_{66} \end{bmatrix}. \tag{14}$$

This matrix is the most general representation of Voigt stiffness matrix. It has 21 independent constants and no rotational invariance with respect to any coordinate axis. It is regarded to possess triclinic symmetry.

The elastic stiffness tensor has monoclinic symmetry when it is invariant under rotation of $180°$ about one coordinate axis (mirror or reflexion symmetry). In this case, the number of independent constants reduces from 21 to 13, and the stiffness matrix has the form as below

$$c_{IJ} = \begin{bmatrix} c_{11} & c_{12} & c_{13} & 0 & c_{15} & 0 \\ c_{12} & c_{22} & c_{23} & 0 & c_{25} & 0 \\ c_{13} & c_{23} & c_{33} & 0 & c_{35} & 0 \\ 0 & 0 & 0 & c_{44} & 0 & c_{46} \\ c_{15} & c_{25} & c_{35} & 0 & c_{55} & 0 \\ 0 & 0 & 0 & c_{46} & 0 & c_{66} \end{bmatrix}. \tag{15}$$

For the case when reflexion symmetries exist with respect to three perpendicular axes, the stiffness matrix has 9 independent constants and said to possess orthorhombic symmetry. It has the following form

$$c_{IJ} = \begin{bmatrix} c_{11} & c_{12} & c_{13} & 0 & 0 & 0 \\ c_{12} & c_{22} & c_{23} & 0 & 0 & 0 \\ c_{13} & c_{23} & c_{33} & 0 & 0 & 0 \\ 0 & 0 & 0 & c_{44} & 0 & 0 \\ 0 & 0 & 0 & 0 & c_{55} & 0 \\ 0 & 0 & 0 & 0 & 0 & c_{66} \end{bmatrix}. \tag{16}$$

The hexagonal symmetry, also known as transversely isotropic symmetry, is the case when the elastic stiffness tensor has one sixfold axis of rotation, i.e., invariant under rotation of $60°$ about one axis. In this case, there are only 5 independent constants in Voigt stiffness matrix as below

$$c_{IJ} = \begin{bmatrix} c_{11} & c_{12} & c_{13} & 0 & 0 & 0 \\ c_{12} & c_{11} & c_{13} & 0 & 0 & 0 \\ c_{13} & c_{13} & c_{11} & 0 & 0 & 0 \\ 0 & 0 & 0 & c_{44} & 0 & 0 \\ 0 & 0 & 0 & 0 & c_{44} & 0 \\ 0 & 0 & 0 & 0 & 0 & c_{66} \end{bmatrix}, \quad \text{with} \quad c_{12} = 2\, c_{66} - c_{11}. \tag{17}$$

For three mutually perpendicular axes of symmetry under a rotation of $90°$ is the case of cubic symmetry. In this case, there are only 3 independent constants, and the elastic stiffness matrix has the form

$$c_{IJ} = \begin{bmatrix} c_{11} & c_{12} & c_{12} & 0 & 0 & 0 \\ c_{12} & c_{11} & c_{12} & 0 & 0 & 0 \\ c_{12} & c_{12} & c_{11} & 0 & 0 & 0 \\ 0 & 0 & 0 & c_{44} & 0 & 0 \\ 0 & 0 & 0 & 0 & c_{44} & 0 \\ 0 & 0 & 0 & 0 & 0 & c_{44} \end{bmatrix}. \tag{18}$$

When the elastic stiffness matrix is invariant under any rotation, it is the case of isotropy. It only has 2 independent constants and no preferential direction. The Voigt stiffness matrix has the following form

$$c_{IJ} = \begin{bmatrix} c_{11} & c_{12} & c_{12} & 0 & 0 & 0 \\ c_{12} & c_{11} & c_{12} & 0 & 0 & 0 \\ c_{12} & c_{12} & c_{11} & 0 & 0 & 0 \\ 0 & 0 & 0 & c_{44} & 0 & 0 \\ 0 & 0 & 0 & 0 & c_{44} & 0 \\ 0 & 0 & 0 & 0 & 0 & c_{44} \end{bmatrix}, \quad \text{with} \quad c_{11} = \, c_{12} + 2\, c_{44}. \tag{19}$$

Lamé's parameters λ and μ of isotropic linear elasticity are, respectively, c_{11} and c_{44}.

An excellent exposition on transformation law for elastic constants and the effect of symmetry are in Bhatia & Singh (1986). For clarity, the interrelation between symmetry and the number of elastic constants are listed in Table 1.

Name	**Number of elastic constants**	**Symmetry**
Triclinic	21	No symmetry axis
Monoclinic	13	One symmetry axis and one mirror plane perpendicular to this axis
Orthorhombic	9	Three symmetry axis and three mirror planes perpendicular to each axis
Hexagonal or transversely isotropic	5	$60°$ of rotation about one axis
Cubic	3	Three mutually perpendicular axes of symmetry for $90°$ rotation
Isotropic	2	Symmetry with respect to all directions.

Table 1: Relation between the number of elastic constants and symmetries.

In the next section, the importance of these symmetries on account of layering and fractures in geological settings is discussed.

2.3 Elastic anisotropy of geological rocks

For a geological material, the arrangements of grains, fractures or bedding in rock formations give rise to anisotropy in the stress and strain relation. Rock formations were created over several millions of years of deposition and diagenesis under the action of tectonic forces. In the subsurface, the settling of sediments, grains and minerals are not random, which results in an ordered distribution.

When rock formation has some symmetry in the arrangements of grains and/or discontinuities, it reduces the number of independent stiffness constants. Based on geological knowledge, one may deduce whether the seismic wave response of a rock formation is likely to be isotropic, transversely isotropic, orthorhombic, or monoclinic, but it will rarely be triclinic. Below the elastic stiffness

tensor corresponding to each symmetry is described and their connection to the arrangements of small-scale heterogeneities is presented.

2.3.1 Monoclinic symmetry

The lowest-symmetry model identified from seismic measurements is monoclinic (Musgrave, 1970; Helbig, 1994). A finely layered medium permeated by a tilted set of fractures manifests itself as monoclinic (Helbig, 2003). This model is important because there is abundant geological evidence of tilted vertical fracture sets.

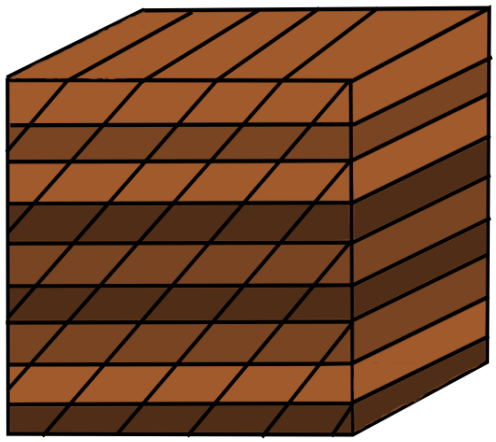

Figure 1: Cartoon of a layered medium permeated by a tilted set of fractures that exhibits monoclinic anisotropy.

2.3.2 Orthorhombic symmetry

This symmetry is characterized by three mirror planes of symmetry and 9 independent elastic constants. Orthorhombic symmetry usually originates from sedimentary basins that are permeated by a set of parallel vertical fractures with vertical transverse isotropy (VTI) in the medium (Ikelle & Amundsen, 2018).

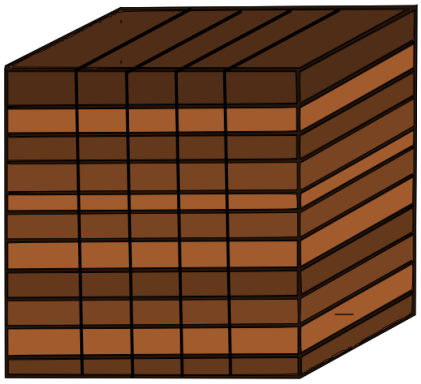

Figure 2: Cartoon of layered medium permeated by orthogonal set of fractures to the lamination that exhibits orthorhombic anisotropy.

2.3.3 Transversely isotropic symmetry

The simplest anisotropic symmetry encountered in hydrocarbon exploration is transverse isotropy or TI. This symmetry implies that the velocities and polarization directions of seismic waves in a given direction vary only with the angle between the direction and the symmetry axis. Typically, this is associated with gravity or regional stress. TI seen by a seismic wave is due to the existence of unidirectional small scale heterogeneities. Typically, that could be because of fine layering of sediments. A finely layered medium permeated by a fracture set that is parallel to the lamination is also TI. A set of parallel fractures in a homogeneous medium also manifest as TI.

If gravity is the principal factor, then the resulting symmetry will be transverse isotropy with a vertical symmetry axis (VTI). On the other hand, if the principal factor are regional stresses then the symmetry axis can be horizontal, resulting in a transverse isotropy with a horizontal symmetry axis (HTI). Also, the symmetry axis can be tilted, resulting in a transverse isotropy with a tilted symmetry axis (TTI). An example of these kinds of mediums are in Figure 3.

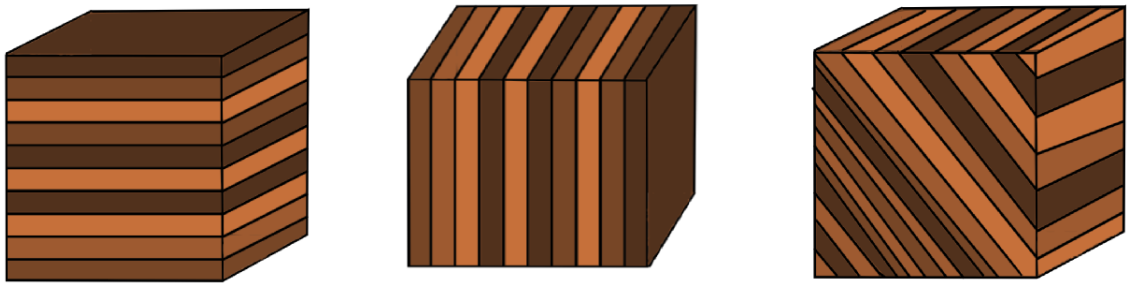

Figure 3: Cartoons of layered media that exhibit transversely isotropic anisotropy. VTI (left), HTI (center) and TTI (right).

A VTI medium can be represented as a layered medium where the physical properties are uniform horizontally but vary vertically and the elastic stiffness matrix c_{IJ} is as equation 17.
A medium with vertical fine layering or fractures manifest HTI anisotropy. For this case, the c_{IJ} stiffness matrix is

$$c_{IJ} = \begin{bmatrix} c_{11} & c_{13} & c_{13} & 0 & 0 & 0 \\ c_{13} & c_{33} & c_{23} & 0 & 0 & 0 \\ c_{13} & c_{23} & c_{33} & 0 & 0 & 0 \\ 0 & 0 & 0 & c_{44} & 0 & 0 \\ 0 & 0 & 0 & 0 & c_{66} & 0 \\ 0 & 0 & 0 & 0 & 0 & c_{66} \end{bmatrix} \tag{20}$$

where $c_{23} = (c_{33} - 2c_{44})$. This symmetry is described with 5 independent constants and 1 dependent constant.

For the cases of dipping transversely isotropic layers, the rock formation has transversely isotropic symmetry with a tilted symmetry axis (TTI) with respect to the surface. To obtain the elastic parameters for this media, matrix 17 or 20 must be rotated in accordance with the orientation of the symmetry axis with respect to vertical azis, i.e., the tilt angle. The elastic stiffness matrix c_{IJ} for

this kind of anisotropy (Ikelle & Amundsen, 2018) is

$$c_{IJ} = \begin{bmatrix} c'_{11} & c'_{12} & c'_{13} & 0 & c'_{15} & 0 \\ c'_{12} & c'_{22} & c'_{23} & 0 & c'_{25} & 0 \\ c'_{13} & c'_{23} & c'_{33} & 0 & c'_{35} & 0 \\ 0 & 0 & 0 & c'_{44} & 0 & c'_{46} \\ c'_{15} & c'_{25} & c'_{35} & 0 & c'_{55} & 0 \\ 0 & 0 & 0 & c'_{46} & 0 & c'_{66} \end{bmatrix} \tag{21}$$

where

$$\begin{aligned}
c'_{11} &= c_{11}\cos^4\theta + 2c_{13}\cos^2\theta\sin^2\theta + c_{33}\sin^4\theta + 4c_{44}\sin^2\theta\cos^2\theta \\
c'_{12} &= c_{12}\cos^2\theta + c_{23}\sin^2\theta \\
c'_{13} &= (c_{11} + c_{33} - 4c_{44})\sin^2\theta\cos^2\theta + c_{13}(\cos^4\theta + \sin^4\theta) \\
c'_{15} &= (c_{13} - c_{33} + 2c_{44})\cos^3\theta\sin\theta + (c_{33} - c_{13} - 2c_{44})\cos\theta\sin^3\theta \\
c'_{22} &= c_{22} \\
c'_{23} &= c_{12}\sin^2\theta + c_{23}\cos^2\theta \\
c'_{25} &= (c_{23} - c_{12})\sin\theta\cos\theta \\
c'_{33} &= c_{11}\sin^4\theta + c_{33}\cos^4\theta + 2(c_{13} + 2c_{44})\cos^2\theta\sin^2\theta \\
c'_{35} &= (c_{13} + 2c_{44} - c_{11})\cos\theta\sin^3\theta + (c_{33} - c_{13} - 2c_{44})\cos^3\theta\sin\theta \\
c'_{44} &= c_{44}\cos^2\theta + c_{66}\sin^2\theta \\
c'_{46} &= c_{44}\cos\theta\sin\theta - c_{66}\cos\theta\sin\theta \\
c'_{55} &= (c_{11} + c_{33} - 2c_{13} - 2c_{44})\cos^2\theta\sin^2\theta + c_{44}(\cos^4\theta + \sin^4\theta) \\
c'_{66} &= c_{66}\cos^2\theta + c_{44}\sin^2\theta
\end{aligned}$$

This symmetry is described by 7 independent elastic parameters and a tilt angle θ of the axis of symmetry. This reduces to VTI when $\theta = 0$ and to HTI when $\theta = 90$.

2.4 Green's function in the k and ω domain

The Fourier transform method is the conventional approach to obtain the Green's function for elastodynamics. Equation 12 is invariant under space and time translations so introducing the nota-

tions, $\mathbf{x}-\mathbf{x}'=\mathbf{r}$ and $t-t'=\tau$, it is

$$\left[\delta_{ip}\,\rho\frac{\partial^2}{\partial t^2}-\frac{\partial}{\partial x_j}c_{ijpq}\frac{\partial}{\partial x_q}\right]G_{pm}\left(\mathbf{r};\tau\right)=\delta_{im}\delta\left(\mathbf{r}\right)\delta\left(\tau\right). \tag{22}$$

Setting the operator

$$\delta_{ip}\,\rho\frac{\partial^2}{\partial t^2}-\frac{\partial}{\partial x_j}c_{ijpq}\frac{\partial}{\partial x_q}\equiv\mathscr{L}_{ip}(\partial), \tag{23}$$

the equation of motion (22), in a compact form, is

$$\mathscr{L}_{ip}\,G_{pm}\left(\mathbf{r};\tau\right)=\delta_{im}\delta\left(\mathbf{r}\right)\delta\left(\tau\right). \tag{24}$$

Using Fourier transformation G_{pm}, $\delta(\mathbf{r})$ and $\delta(\tau)$ are

$$G_{pm}(\mathbf{r},\tau) = \frac{1}{2\pi}\int_{-\infty}^{\infty}d\omega\,\frac{1}{(2\pi)^3}\int_{-\infty}^{\infty}d^3\mathbf{k}\,\tilde{G}_{pm}(\mathbf{k};\omega)\,e^{i(\mathbf{k}\cdot\mathbf{r}-\omega\tau)}, \tag{25}$$

$$\delta(\mathbf{r}) = \frac{1}{(2\pi)^3}\int_{-\infty}^{\infty}d^3\mathbf{k}\,e^{-i\,\mathbf{k}\cdot\mathbf{r}}, \tag{26}$$

$$\delta(\tau) = \frac{1}{2\pi}\int_{-\infty}^{\infty}d\omega\,e^{-i\omega\tau}. \tag{27}$$

Substituting equations (25), (26) and (27) in equation (22) one obtains an algebraic equation

$$\underbrace{\left(c_{ijpq}k_jk_q-\delta_{ip}\rho\omega^2\right)}_{\tilde{\mathscr{L}}_{ip}}\tilde{G}_{pm}=\delta_{im}. \tag{28}$$

$\tilde{\mathscr{L}}_{ip}$ is known as the Green's Christoffel matrix. From equation (28) it is apparent that $\tilde{\mathscr{L}}_{ip}$ is the inverse of $\tilde{G}_{ip}$. Therefore, the Green's function in wave-number frequency domain is

$$\tilde{G}_{pm}=\tilde{\mathscr{L}}_{pm}^{-1}=\frac{\tilde{\mathscr{L}}_{pm}^{\dagger}}{\Delta_{\mathscr{L}}} \tag{29}$$

where $\tilde{\mathscr{L}}_{pm}^{\dagger}$ is the cofactor transpose and $\Delta_{\mathscr{L}}$ is the determinant of the Green's Christoffel matrix $\tilde{\mathscr{L}}_{pm}$. To return to a spatial-temporal domain the inverse Fourier transformation (25) is applied, which yields

$$G_{pm}(\mathbf{r},\tau) = \frac{1}{2\pi}\int_{-\infty}^{\infty}d\omega\,\frac{1}{(2\pi)^3}\int_{-\infty}^{\infty}d^3\mathbf{k}\,\frac{\tilde{\mathscr{L}}_{pm}^{\dagger}}{\Delta_{\mathscr{L}}}\,e^{i(\mathbf{k}\cdot\mathbf{r}-\omega\tau)}. \tag{30}$$

This inverse transformation involves infinite integrals over wave-numbers and frequency, which are tedious to evaluate because the integration kernel has singularities and branch cuts, except for the isotropic case.

For the isotropic case, the stiffness tensor is defined as

$$c_{ijpq} = \lambda \delta_{ij} \delta_{pq} + \mu \left(\delta_{ip} \delta_{jq} + \delta_{iq} \delta_{jp} \right), \tag{31}$$

with which

$$\tilde{G}_{pm}(\mathbf{k}, \omega) = \frac{1}{\left(\mu \mathbf{k}^2 - \rho \omega^2 \right)} \left[\delta_{pm} - \frac{\left(\lambda + \mu \right) k_p k_m}{\left(\lambda + 2\mu \right) \mathbf{k}^2 - \rho \omega^2} \right]. \tag{32}$$

Introducing velocities

$$\alpha = \sqrt{\frac{\lambda + 2\mu}{\rho}}, \qquad\qquad \beta = \sqrt{\frac{\mu}{\rho}}, \tag{33}$$

where α is the velocity of the P-wave or compressional wave and β is the velocity of the S-wave or shear wave, equation (32) becomes

$$\tilde{G}_{pm}(\mathbf{k}, \omega) = \frac{1}{\rho(\beta^2 \mathbf{k}^2 - \omega^2)} \left[\delta_{pm} - \frac{\left(\alpha^2 - \beta^2 \right) k_p k_m}{\alpha^2 \mathbf{k}^2 - \omega^2} \right]. \tag{34}$$

Applying inverse Fourier transform to go to a physical domain $\mathbf{x}$ and t domain, the Green's function for isotropic case is

$$\begin{aligned} G_{pm}(\mathbf{r}, \tau) &= \frac{1}{4\pi\rho\alpha^2} \frac{\delta(\tau - t_\alpha)}{\mathbf{r}} \gamma_p \, \gamma_l + \frac{1}{4\pi\rho\beta^2} \frac{\delta(\tau - t_\beta)}{\mathbf{r}} \left(\delta_{pm} - \gamma_p \, \gamma_l \right) \\ &+ \frac{1}{4\pi\rho} \frac{3\gamma_p \gamma_l - \delta_{pl}}{\mathbf{r}^3} \tau \left(\Theta \left(\tau - t_\alpha \right) - \Theta \left(\tau - t_\beta \right) \right) \end{aligned} \tag{35}$$

where $t_\alpha = \frac{\mathbf{r}}{\alpha}$, $t_\beta = \frac{\mathbf{r}}{\beta}$ are, respectively, the travel time for P- and S-waves and $\gamma_j = \frac{r_j}{|\mathbf{r}|}$ are the direction cosines of the line from source to point of observation.

Chapter 3 Closed-form solution for the anisotropic Green's function

This chapter develops the closed-form solution for the anisotropic Green's function using the Radon transform approach as in Wang & Achenbach (1995). This solution is the integration over a unit sphere of a kernel that is composed of the eigenvalues and eigenvectors of the Kelvin-Christoffel matrix of the anisotropic elasticity. First, in §3.1, a brief introduction of the Radon transform is presented. The solution to the 3-D Helmholtz equation is developed in §3.2, to illustrate this methodology. The closed-form solution for general anisotropic wave equation using the Radon transform is presented in §3.3. Gaussian quadrature is used to evaluate this integral, which is implemented in MatLab. The details of this numerical evaluation are in §3.4.

3.1 The Radon transform

3.1.1 Preliminaries

The Radon transform is the projection of a function to a hyperplane. A hyperplane is a subspace which reduces one dimension of its ambient space. For 3-dimensional space, its hyperplanes are 2-dimensional planes. Likewise, for 2-dimensional space, its hyperplanes are 1-dimensional lines. This transformation is extensively used for reconstructing images in X-ray computed tomography.

An interesting feature of the Radon transform is that it reduces a 3-D partial differential equation to a 1-D differential equation. This property of Radon transform is utilized for solving the anisotropic Green function problem.

Let $\mathbf{x} = (x_1, x_2, x_3)$ be the coordinates of a point in the space R^3 and consider some function $f(\mathbf{x})$ defined in R^3. The Radon transform of $f(\mathbf{x})$ is defined as

$$\hat{f}(s, \mathbf{n}) = R[f(\mathbf{x})] = \int f(\mathbf{x})\delta(s - \mathbf{n} \cdot \mathbf{x})d\mathbf{x}. \tag{36}$$

Thus, the Radon transform is an integration of $f(\mathbf{x})$ over all planes defined by $\mathbf{n} \cdot \mathbf{x} = s$, where $\mathbf{n}$ is the unit normal vector to the plane. The inverse Radon transformation is carried out in two steps. First, one needs to obtain the second derivative of the function in s domain

$$\overline{f}(s, \mathbf{n}) = \partial_s^2 \hat{f}(s, \mathbf{n}), \tag{37}$$

and the next step is the integration over the unit sphere

$$f(\mathbf{x}) = -\frac{1}{8\pi^2} \int_{|\mathbf{n}|=\mathbf{1}} \overline{f}(\mathbf{n} \cdot \mathbf{x}, \mathbf{n}) dS(\mathbf{n}). \tag{38}$$

The inverse Radon transform is expressed in terms of an integral over the unit sphere (in 3 dimensions) or a line integral over a unit circle (in 2 dimensions). The procedure for integrating over unit sphere is presented in the next section.

3.1.2 Integration over unit sphere

Let $\mathbf{e}$ be the unit vector in the direction of the point of observation $\mathbf{x}$ (see Figure 4), i.e. it is the direction of the radius vector. Thus for $|\mathbf{x}| = r$,

$$\mathbf{x} = r\mathbf{e}. \tag{39}$$

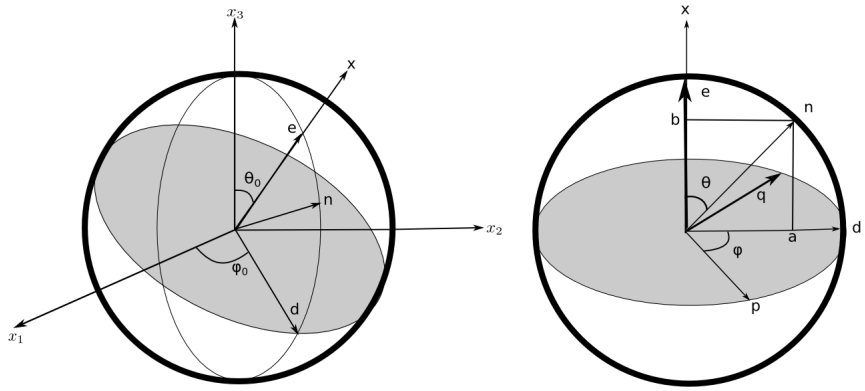

Figure 4: (Left) Illustration of vectors $\mathbf{x}, \mathbf{e}, \mathbf{d}$ and $\mathbf{n}$ in the fixed x_i coordinates. (Right) Relation between these vectors on the unit circle.

Let there be a unit vector $\mathbf{d}$ normal to the direction of $\mathbf{x}$. Thus,

$$\mathbf{d} \cdot \mathbf{e} = 0 \tag{40}$$

Then a unit vector $\mathbf{n}$ is defining the plane

$$\mathbf{n} = a\mathbf{d} + b\mathbf{e}, \tag{41}$$

where $a = \sqrt{1-b^2}$. From equations 40 and 41, we have

$$\mathbf{n} \cdot \mathbf{x} = (a\mathbf{d} + b\mathbf{e}) \cdot r\mathbf{e} = rb. \tag{42}$$

From Figure 4 we can define function $\mathbf{d}$ as a function of ϕ given by

$$\mathbf{d}(\phi) = \cos\phi\mathbf{p} + \sin\phi\mathbf{q} \tag{43}$$

where $\mathbf{p}$ and $\mathbf{q}$ are a set of orthonormal vectors in the plane normal to $\mathbf{e}$ (see Figure 4).

Using the coordinate system (e, p, q), we can determine the values of the normal vector $\mathbf{n}$ in terms of the b and θ plane where the components of the $\mathbf{n}$ vector can be defined as

$$\begin{aligned} n_1 &= b\,, \\ n_2 &= \sqrt{1-b^2}\cos\theta, \\ n_3 &= \sqrt{1-b^2}\sin\theta. \end{aligned}$$

Then a unit vector $\mathbf{n}$ defining the plane of integration over unit sphere with respect to b and θ, from Figure 4, yields

$$f(\mathbf{x}) = -\frac{1}{8\pi^2}\int_0^{2\pi}\int_{-1}^{1} \overline{f}[rb, \mathbf{n}(b, \mathbf{d}(\phi))]dbd\phi \tag{44}$$

3.1.3 Some properties of Radon transform

The following properties of $\hat{f}$ are inmediate consequences of the definition given in equation (36)

homogeneity: $$\hat{f}(\alpha s, \alpha\mathbf{n}) = |\alpha|^{-1}\hat{f}(x, \mathbf{n}) \tag{45}$$

linearity: $$\mathbf{R}(c_1 f + c_2 g) = c_1\hat{f} + c_2\hat{g} \tag{46}$$

transform of derivatives: $$\mathbf{R}(\partial_i f(\mathbf{x})) = n_i \partial_s \hat{f}(s, \mathbf{n}) \tag{47}$$

3.2 Solution of 3-D Helmholtz equation using the Radon transform

As an exercise in using the Radon transform the Green's function for the 3-D scalar wave equation is constructed. Taking the Fourier transform with respect to time of the wave equation, the 3-D Helmholtz equation is obtained as

$$[K(\partial_1^2 + \partial_2^2 + \partial_3^2) + \rho\omega^2]G(\mathbf{x};\omega) = -\delta(\mathbf{x}) \tag{48}$$

where K, $G(\mathbf{x};\omega)$ and $\delta(\mathbf{x})$ are a positive constant, the Green Function and the force term, respectively.

Applying the Radon transformation, the above equation reduces to

$$[K\partial_s^2 + \rho\omega^2]\hat{G}(s) = -\delta(s). \tag{49}$$

This equation shows how Radon transform reduces the 3-D Helmholtz equation to a 1-D Helmholtz equation.

The outgoing wave solution in the s coordinate, generated by the source $\delta(s)$, is in the form

$$\hat{G} = \frac{i}{2\rho c^2 k} e^{ik|s|}, \tag{50}$$

where c and k are the phase velocity and the wave number given by

$$c = \sqrt{\frac{K}{\rho}}, \qquad \text{and} \qquad k = \frac{\omega}{c}. \tag{51}$$

The second derivative of the Green's Function in Radon domain is

$$\overline{G}(s, \mathbf{n}) = \partial_s^2 \hat{G} = \frac{i}{2\rho c^2 k} \partial_s^2 e^{ik|s|} = \frac{-1}{2\rho c^2}[2\delta(s) + ike^{ik|s|}] \tag{52}$$

Therefore we may write

$$\overline{G}(\mathbf{n}\cdot\mathbf{x},\mathbf{n}) = -\frac{ik}{2\rho c^2}e^{ik|\mathbf{n}\cdot\mathbf{x}|} - \frac{1}{\rho c^2}\delta(\mathbf{n}\cdot\mathbf{x}) \tag{53}$$

where the first term is the regular part G^R of the function and the second term is the singular part G^S. Using the inverse Radon formula (38) we have,

$$G(\mathbf{x},\omega) = -\frac{1}{8\pi^2}\int_{|\mathbf{n}|=\mathbf{1}}\left(-\frac{ik}{2\rho c^2}e^{ik|\mathbf{n}\cdot\mathbf{x}|} - \frac{1}{\rho c^2}\delta(\mathbf{n}\cdot\mathbf{x})\right)dS(\mathbf{n}),. \tag{54}$$

Where the regular part and singular part of this integral are

$$G^R(\mathbf{x},\omega) = \frac{ik}{16\pi^2\rho c^2}\int_0^{2\pi}d\phi\int_{-1}^{1}e^{ikr|b|}db \tag{55}$$

and

$$G^S(\mathbf{x}) = \frac{1}{8\pi^2\rho c^2}\int_0^{2\pi}d\phi\int_{-1}^{1}\delta(rb)db, \tag{56}$$

respectively. Evaluating the integrals 55 and 56 yields

$$G^R(\mathbf{x},\omega) = \frac{1}{4\pi\rho c^2}\frac{e^{ikr}-1}{r} \tag{57}$$

and

$$G^S(\mathbf{x}) = \frac{1}{4\pi\rho c^2}\frac{1}{r}. \tag{58}$$

The final solution is

$$G(\mathbf{x},\omega) = G^S + G^R = \frac{1}{4\pi\rho c^2}\frac{e^{ikr}}{r}. \tag{59}$$

Note that $G^R(\mathbf{x})$ is a regular function and $G^R(\mathbf{x}) \to 0$ when $\omega \to 0$. $G^S(\mathbf{x})$ correspond to the static Green's function which is not frequency dependent.

3.3 Radon transform approach for the anisotropic Green's function

From expression (12) , the Green's function for the equation of motion in frequency domain is

$$\left[\delta_{ip}\,\rho\omega^2 + \frac{\partial}{\partial x_j} c_{ijpq} \frac{\partial}{\partial x_q}\right] G_{pm}\left(\mathbf{x};\omega\right) = -\delta_{im}\delta\left(\mathbf{x}\right).$$

Introducing the notation $\frac{\partial}{\partial x_j} c_{ijpq} \frac{\partial}{\partial x_q} \equiv \Gamma_{ip}$, the above is written as

$$\left[\Gamma(\partial) + \rho\omega^2\delta_{ip}\right] \tilde{G}_{pm}(\mathbf{x},\omega) = -\delta_{im}\delta(\mathbf{x}). \tag{60}$$

Γ_{ip} is known as Kelvin-Christoffel operator. Using Voigt notation for stiffness tensor, c_{ijpq}, the operator Γ_{ip} is

$$\Gamma(\partial) = \mathscr{E}\; c_{_{IJ}}\; \mathscr{E}^T, \tag{61}$$

where $\mathscr{E}$ is the operator

$$\mathscr{E}(\partial) = \begin{bmatrix} \partial_1 & 0 & 0 \\ 0 & \partial_2 & 0 \\ 0 & 0 & \partial_3 \\ 0 & \partial_3 & \partial_2 \\ \partial_3 & 0 & \partial_1 \\ \partial_2 & \partial_1 & 0 \end{bmatrix}. \tag{62}$$

The Radon transformation of operator $\mathscr{E}$ reads as

$$\hat{\mathscr{E}}(s,\mathbf{n}) = \underbrace{\begin{bmatrix} n_1 & 0 & 0 \\ 0 & n_2 & 0 \\ 0 & 0 & n_3 \\ 0 & n_3 & n_2 \\ n_3 & 0 & n_1 \\ n_2 & n_1 & 0 \end{bmatrix}}_{\mathbf{P}} \partial_s \tag{63}$$

The Kelvin-Christoffel operator transforms into the Radon domain as

$$\mathscr{R}[\Gamma] \equiv \underbrace{\mathbf{P}\ c_{IJ}\ \mathbf{P}^T}_{\hat{\Gamma}} \partial_s^2, \tag{64}$$

thereby, the Green's function (60) transforms in Radon domain to

$$\left[\hat{\Gamma}_{ip}(\mathbf{n})\partial_s^2 + \rho\omega^2\delta_{ip}\right]\hat{G}_{pk} = -\delta_{ik}\delta(s). \tag{65}$$

The above is a system of three coupled 1-D Helmholtz equations. In order to uncoupled this system of equations, $\Gamma_{ip}(\mathbf{n})$ is decomposed in terms of its eigenvalues λ_m and eigenvectors E_{im} as

$$\Gamma_{ip}(\mathbf{n})E_{pm} = \lambda_m E_{im} \tag{66}$$

where the eigenvectors have real orthonormal bases and the eigenvalues are all real numbers due to the symmetry of the Kelvin-Christoffel operator. The summation convention does not apply to the suffix, m, whenever λ_m, or later on, in other two values (c_m and k_m). The transformation of the Green's function to this new basis are given by

$$\hat{\mathbf{G}}'_{mk} = E_{pm}\hat{\mathbf{G}}_{pk}, \tag{67}$$

and the inverse transformation is

$$\hat{\mathbf{G}}_{pk} = E_{pn}\hat{\mathbf{G}}'_{nk}. \tag{68}$$

The transformation of equation (60), by operating the eigenvectors E_{im} on both sides of the equation and using the transformation for the Green's function, follows

$$\left[E_{im}\hat{\Gamma}_{ip}(\mathbf{n})E_{pn}\partial_s^2 + \rho\omega^2 E_{im}\delta_{ip}E_{pn}\right]\hat{G}'_{nk} = -E_{im}\delta_{ik}\delta(s). \tag{69}$$

Denoting that

$$E_{im}\hat{\Gamma}_{ip}(\mathbf{n})E_{pn} = E_{im}\lambda_n E_{in} = \lambda_n E_{im}E_{in} = \lambda_m\delta_{mn}, \tag{70}$$

and

$$E_{im}\delta_{ip}E_{pn} = E_{im}E_{in} = \delta_{mn}, \tag{71}$$

equation (69) corresponds to the following set of three uncoupled equations

$$\left[\lambda_m \partial_s^2 + \rho\omega^2\right] \hat{G'}_{mk} = -E_{km}\delta(s). \tag{72}$$

The solution corresponding to an outgoing wave is given by

$$\hat{G'}_{mk} = \frac{iE_{km}}{2\rho c_m^2 k_m} e^{ik_m|s|}, \tag{73}$$

where c_m and k_m are, respectively, the phase velocities and the wavenumber defined by

$$c_m = \sqrt{\frac{\lambda_m}{\rho}}, \tag{74}$$

and

$$k_m = \frac{\omega}{c_m}. \tag{75}$$

Applying the transformation to revert to $\hat{G}_{pk}$ in (73) yields

$$\hat{G}_{pk} = \sum_{m=1}^{3} \frac{iE_{pm}E_{km}}{2\rho c_m^2 k_m} e^{ik_m|s|}. \tag{76}$$

To use the inverse Radon transform, the second derivative is

$$\bar{G}_{pk}(s, \mathbf{n}) = \partial_s^2 \hat{G}_{pk} = \sum_{m=1}^{3} \frac{-E_{pm}E_{km}}{2\rho c_m^2} \left(2\delta(s) + ik_m e^{ik_m|s|}\right). \tag{77}$$

Applying the inverse Radon transform to equation (76) we have Green's function in frequency domain

$$G_{pk}(\mathbf{x}, \omega) = -\frac{1}{8\pi^2} \int_{|\mathbf{n}|=\mathbf{1}} \bar{G}_{pk}(s, \mathbf{n}) dS(\mathbf{n}). \tag{78}$$

$G_{pk}(\mathbf{x}, \omega)$ has a regular part $G_{pk}^R(\mathbf{x}, \omega)$ and a singular part $G_{pk}^S(\mathbf{x}, \omega)$ as

$$G_{pk}(\mathbf{x}, \omega) = G_{pk}^R(\mathbf{x}, \omega) + G_{pk}^S(\mathbf{x}, \omega). \tag{79}$$

The regular part is

$$G^R_{pk}(\mathbf{x},\omega) = \frac{i}{8\pi^2}\int_{|\mathbf{n}|=1}\sum_{m=1}^{3}\frac{k_m E_{pm}E_{km}}{2\rho c_m^2}e^{ik_m|\mathbf{n}\cdot\mathbf{x}|}dS(\mathbf{n}) \tag{80}$$

and the singular part is

$$G^S_{pk}(\mathbf{x},\omega) = \frac{1}{8\pi^2}\int_{|\mathbf{n}|=1}\sum_{m=1}^{3}\frac{E_{pm}E_{km}}{\rho c_m^2}\delta(\mathbf{n}\cdot\mathbf{x})dS(\mathbf{n}). \tag{81}$$

Hence, summing these two equations, yields the Green function in frequency domain as

$$G_{pk}(\mathbf{x},\omega) = \frac{i}{8\pi^2}\int_{|\mathbf{n}|=1}\sum_{m=1}^{3}\frac{k_m E_{pm}E_{km}}{2\rho c_m^2}e^{ik_m|\mathbf{n}\cdot\mathbf{x}|}dS(\mathbf{n}) + \frac{1}{8\pi^2}\int_{|\mathbf{n}|=1}\sum_{m=1}^{3}\frac{E_{pm}E_{km}}{\rho c_m^2}\delta(\mathbf{n}\cdot\mathbf{x})dS(\mathbf{n}) \tag{82}$$

For the isotropic case, the integrals can be analytically integrated. However, for anisotropy, these integrals need to be numerically evaluated.

3.3.1 Numerical integration by Gaussian quadrature method

The closed-form solution (82) requires numerical integration over a unit sphere. For this purpose, the numerical evaluation of integrals is carried out using the Gaussian quadrature method.

Numerical integration formulas are developed by fitting approximating functions to discrete data and integrating an approximation function

$$I = \int_a^b f(x)dx \cong \int_a^b P_n(x)dx. \tag{83}$$

The above representation is illustrated in Figure 5

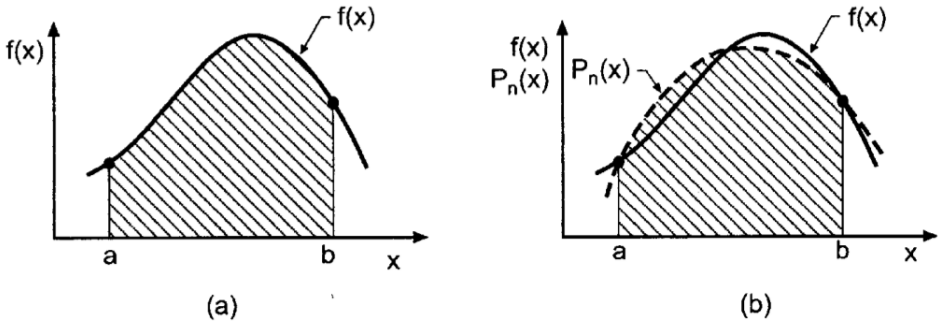

Figure 5: Numerical integration. (a) Exact integral. (b) Approximate integral. (Adopted from Hoffman (1992)).

Gaussian quadrature method is an approximate method of calculating an integral

$$I = \int_a^b f(x)dx = \sum_{i=1}^{n} C_i f(x_i), \tag{84}$$

by choosing the values of x_i and C_i in (84) so that the integral of the polynomial is exact. x_i are the locations at which the integrand function $f(x)$ is known and C_i are weighting factors. Above equation can be transformed from x space to t space by the transformation

$$x = mt + c, \tag{85}$$

where

$$m = \frac{b-a}{2}, \qquad \text{and} \qquad c = \frac{b+a}{2}, \tag{86}$$

Thus, integral (84) becomes

$$I = \int_a^b f(x)\ dx = \int_{-1}^{1} f(x(t))\ dt = \int_{-1}^{1} f(mt+c)\ m\ dt. \tag{87}$$

Substituting expression(86) into 87 yields

$$I = \frac{b-a}{2} \int_{-1}^{1} F(t)dt \tag{88}$$

where $F(t) = f(mt + c)$.

For higher-order formulas the expression is the following

$$\int_a^b f(x)dx \approx \frac{b-a}{2}\sum_{i=1}^{n} C_i F(t_i) \tag{89}$$

n	**Values of t_i**	**Values of C_i**	**Order**
2	$\frac{-1}{\sqrt{3}}$	1	3
	$\frac{1}{\sqrt{3}}$	1	
3	$-\sqrt{0.6}$	$\frac{5}{9}$	5
	0	$\frac{8}{9}$	
	$\sqrt{0.6}$	$\frac{5}{9}$	
4	-0.8611363116	0.3478548451	7
	-0.3399810436	0.6521451549	
	0.3399810436	0.6521451549	
	0.861136311	0.347854845	

Table 2: Gaussian quadrature parameters.

Table 2 presents t_i and C_i for $n = 2, 3$ and 4. Other higher-order results are presented by Abramowitz & Stegun (1964).

Equation (82) requires the use of a double Gaussian quadrature to obtain the numerical result of a double integral. To implement this integration method, the following pseudo-code is presented where $input\_C$ represents the parameters of the stiffness matrix and the density of the medium. ω is the value of the frequency.

This program solves in each section all the contribution of inner integral and then evaluates in each part of the outer integral. The final result is the addition of every section of the regular and singular part of the closed-form solution(82).

Algorithm 1 Gaussian Quadrature algorithm for anisotropic solids.

function GAUSSIANQUADRATURE($input\_C$, ω)
  GIVE NUMBER OF SECTIONS FOR EACH INTEGRAL
  GIVE VALUES FOR GAUSSIAN QUADRATURE
  for $sections1 \leftarrow 1, k$ **do**
    $integralresult2 = 0$
    for $sections2 \leftarrow 1, h$ **do**
      $integralresult3 = 0$
      for $sections3 \leftarrow 1, n$ **do**
        $integralresult4 = 0$
        for $sections4 \leftarrow 1, i$ **do**
          $theta = mt(n) * tint(i) + dtheta(n)$
          $b = mb(k) * tint(h) + db(k)$
          KC=SET UP THE KELVIN-CHRISTOFFEL MATRIX
          $[EV, EG]$ =OBTAIN EIGENVALUES AND EIGENVECTORS OF KC
          F=ELABORATE THE FUNCTION INTEGRALS USING [EV,EG]
          $integralresult4 = integralresult4 + coeff(i) * F$
        end for
        $integralresult3 = integralresult3 + mt(n) * integralresult4$
      end for
      $integralresult2 = integralresult2 + coeff(h) * integralresult3$
    end for
    $integralresult1 = integralresult1 + mb(k) * integralresult2$
  end for
  FINAL RESULT= $integralresult1$

The MatLab code generated in this work allows to obtain the Green's function for all classes of anisotropy only changing the elastic constants of KC.

Chapter 4 Numerical solution for the anisotropic Green's function

In this chapter, the numerical solution for isotropic, transversely isotropic, orthorhombic and monoclinic symmetry are obtained using the Radon transform approach. The symmetry axis is taken always along x_3 axis. The validation of this approach is accomplish by comparing the exact solution with the numerical solution in the isotropic symmetry in §4.1. The comparison of the pure direction velocities, i.e., the direction which the wave solutions become pure transverse or pure longitudinal (Auld, 1973), and the numerical solution is other validation presented in §4.2. The receiver locations are along x_1 axis. From §4.3 to §4.5, numerical solution for different anisotropic symmetries are presented. In §4.6, the radiation patterns for TI case in (x_1, x_3) plane is shown. They show the shear wave splitting and the directional dependence of waves velocities. The computation of wave-fields in time domain is carried out by band limiting the source pulse as a Ricker wavelet, so that a fast Fourier transform scheme is applicable.

4.1 Validation with the analytical solution in isotropic medium

For the validation of this methodology, the comparison of the analytical solution with the numerical solution for isotropic case is presented here. The results of computing expression (82) to applying a force in the origin and measuring waves in G_{11} for this symmetry are computed here using Gaussian quadrature. Parameters of the medium are in Table 3.

Parameters	**Values**
c_{11}	$6.3667\ \mathrm{GPa}$
c_{44}	$2.3000\ \mathrm{GPa}$
c_{12}	$1.7667\ \mathrm{GPa}$
ρ	$2650\ \mathrm{kg/m^3}$
r_0	$1000\ \mathrm{m}$

Table 3: List of parameters for isotropic case. r_0 corresponds to the distance between source and receiver.

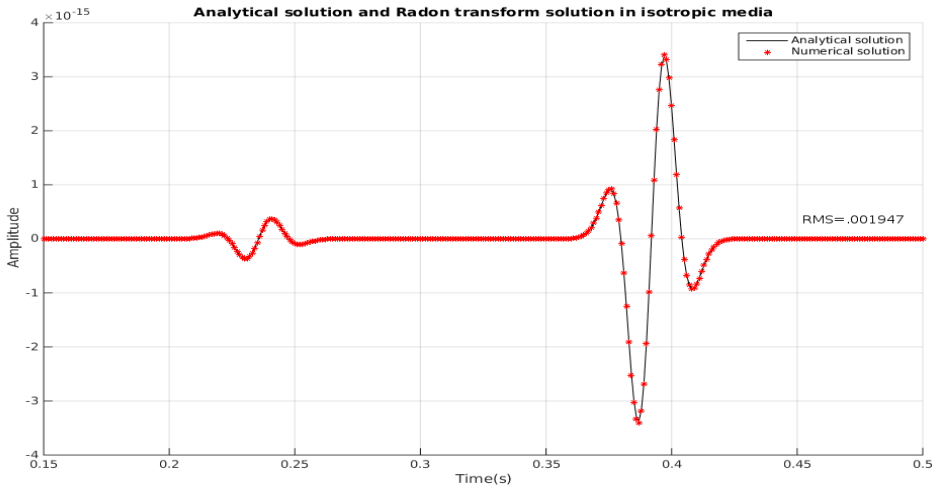

Figure 6: Comparison between analytical solution and numerical solution in isotropic medium.

Figure 6 shows similarity between the analytical and the numerical solution. The P- and S-waves are clearly observed, for which analytical formulas are

$$v_p = \sqrt{\frac{c_{11}}{\rho}} \qquad \text{and} \qquad v_s = \sqrt{\frac{c_{44}}{\rho}}.$$

Observed velocities are compared with the analytical velocities in Table 4.

Velocity	Analytical solution	Numerical solution
v_p	4.90×10^3 m/s^2	4.89×10^3 m/s^2
v_s	2.94×10^3 m/s^2	2.93×10^3 m/s^2

Table 4: Comparison of velocities for isotropic case.

From this experiment, it can be concluded that the comparison of the velocities and waveforms for P- and S-waves in isotropic medium are acceptable.

4.2 Validation with pure direction velocities in transversely isotropic medium

Another validation for this methodology is comparing the pure direction velocities in VTI and HTI symmetries. Next results present the numerical solution for these symmetries applying a force in the origin and measuring waves in G_{11} .The parameters of the medium are given in Table 5.

Parameters	Values
c_{11}	13.8 GPa
c_{44}	3.20 GPa
c_{13}	5.80 GPa
r_0	400 m
$\#\ geophones$	4

Parameters	Values
c_{33}	15.0 GPa
c_{12}	7.10 GPa
ρ	916.8 kg/m^3
Δr	300 m

Table 5: List of parameters for transversely isotropic case. This parameters correspond to a cubic ice with hexagonal symmetry. r_0, Δr and $\#\ geophones$ are, respectively, the distance between source and first receiver, the increment of distance between each receiver, and the number of geophones.

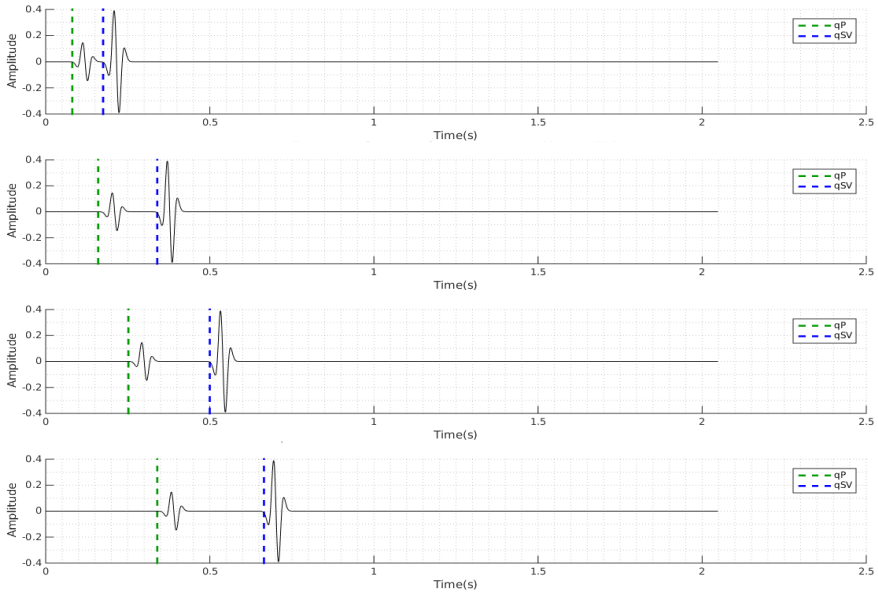

Figure 7: Scaled displacement (by c_{44} parameter) measured in pure direction of VTI symmetry. The geophones are located in 400m., 700m., 1000m. and 1300m. Source is a Ricker pulse of amplitude 1.

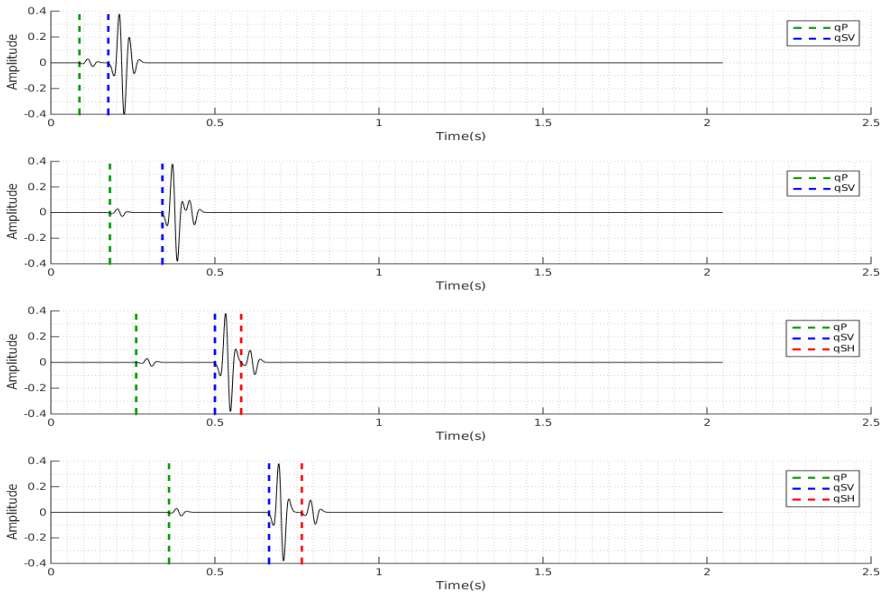

Figure 8: Scaled displacement (by c_{44} parameter) measured in pure direction of HTI symmetry. The geophones are located in 400m., 700m., 1000m. and 1300m. Source is a Ricker pulse of amplitude 1.

In Figures 7 and 11, we can observe the behavior of qP-, qSV- and qSH-waves with respect to distance using the parameters of Table 5. The velocities can be compared with

$$\begin{aligned} v_{qP}^2 &= \frac{1}{2\rho}[c_{33}+c_{44}+(c_{11}-c_{33})\sin^2\theta + D(\theta)] \\ v_{qSV}^2 &= \frac{1}{2\rho}[c_{33}+c_{44}+(c_{11}-c_{33})\sin^2\theta - D(\theta)] \\ v_{qSH}^2 &= \frac{1}{\rho}[c_{66}\sin^2\theta + c_{44}\cos^2\theta] \end{aligned} \tag{90}$$

where

$$\begin{aligned} D(\theta) &= [(c_{33}-c_{44})^2 + 2[(c_{13}+c_{44})^2 - (c_{33}-c_{44})(c_{11}+c_{33}-2c_{44})]\sin^2\theta \\ &+ [(c_{11}+c_{33}-2c_{44})^2 - 4(c_{13}+c_{44})^2]\sin^4\theta]^{\frac{1}{2}} \end{aligned} \tag{91}$$

given in Thomsen (2002). This formulas predicts the velocities of these three waves. The pure

velocities is obtained by setting $\theta = 0$ and $\theta = 90$ degrees in the above formulas, which yields

$$\begin{aligned} v_{qP}(0°) &= \sqrt{\frac{c_{33}}{\rho}} \\ v_{qSV}(0°) &= \sqrt{\frac{c_{44}}{\rho}} \\ v_{qSH}(0°) &= \sqrt{\frac{c_{44}}{\rho}} \end{aligned} \tag{92}$$

and

$$\begin{aligned} v_{qP}(90°) &= \sqrt{\frac{c_{11}}{\rho}} \\ v_{qSV}(90°) &= \sqrt{\frac{c_{44}}{\rho}} \\ v_{qSH}(90°) &= \sqrt{\frac{c_{66}}{\rho}}. \end{aligned} \tag{93}$$

From this analytical solutions, is easy to derive that in 0 degrees only two wavefronts are observed. The first wavefront includes the qP-wave and the second wavefront includes qSV- and qSH-waves. For 90 degrees, it can be observed the splitting of S-wave corresponding to a HTI symmetry. These phenomena can be observed in Figures 7 and 11. Numerical values compared with analytical velocities in Table 6 for VTI and in Table 7 for HTI.

Velocity	**Analytical**	**Numerical**
qP	$4.04 \times 10^3\ \mathrm{m/s^2}$	$4.02 \times 10^3\ \mathrm{m/s^2}$
qSV	$1.86 \times 10^3\ \mathrm{m/s^2}$	$1.84 \times 10^3\ \mathrm{m/s^2}$
qSH	$1.86 \times 10^3\ \mathrm{m/s^2}$	$1.84 \times 10^3\ \mathrm{m/s^2}$

Table 6: Comparison of velocities for VTI medium.

Velocity	**Analytical**	**Numerical**
qP	$3.87 \times 10^3\ \mathrm{m/s^2}$	$3.84 \times 10^3\ \mathrm{m/s^2}$
qSV	$1.86 \times 10^3\ \mathrm{m/s^2}$	$1.84 \times 10^3\ \mathrm{m/s^2}$
qSH	$1.89 \times 10^3\ \mathrm{m/s^2}$	$1.88 \times 10^3\ \mathrm{m/s^2}$

Table 7: Comparison of velocities for HTI medium.

These results show the effectiveness of this methodology and a validation for the MatLab code developed in this thesis.

4.3 Numerical solution for the anisotropic Green's function in VTI symmetry

The results of evaluating 82 by applying a force in the origin and measuring waves in G_{11}, G_{22} and G_{33} for VTI symmetry are computed here using Gaussian Quadrature. The parameters of the medium are given in Table 8.

Parameters	Values	Parameters	Values
c_{11}	34.3 GPa	c_{12}	13.1 GPa
c_{13}	10.7 GPa	c_{33}	22.7 GPa
c_{44}	5.40 GPa	c_{66}	10.6 GPa
r_0	900 m	ρ	2060.8 kg/m^3

Table 8: List of parameters for VTI symmetry. The elastic constants correspond to a Cretaceous shale taken from Ikelle & Amundsen (2018).

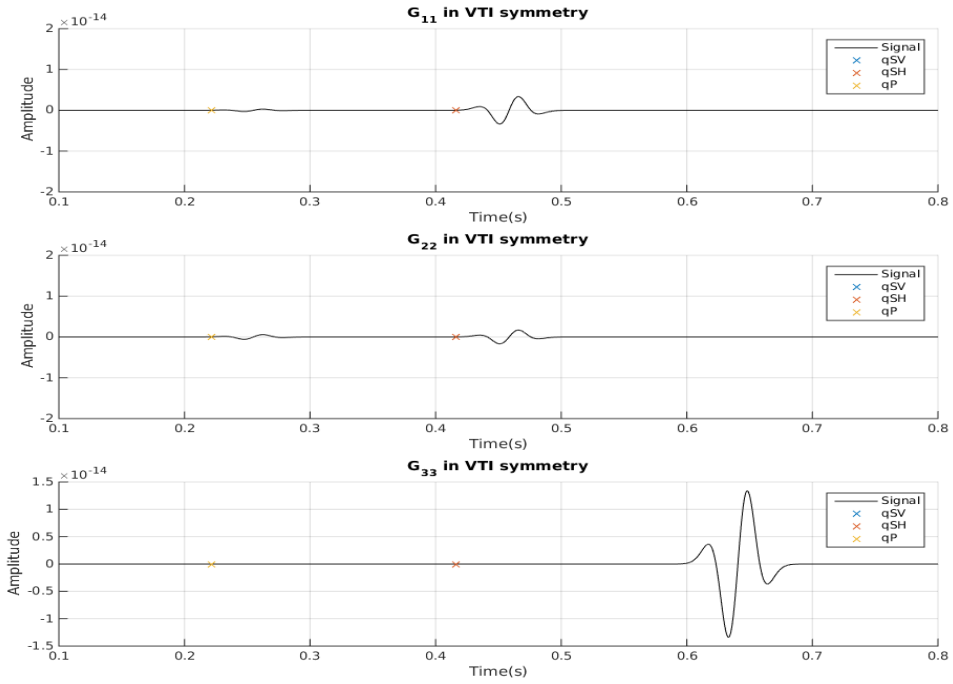

Figure 9: G_{11}, G_{22} and G_{33} solutions for VTI symmetry. The color marks correspond to the travel time of the first arrival of the wavefields.

The analytical travel time shows the existence of two anisotropic waves, qP and qSV, and the numerical solution agrees with this solution. The comparison of analytical travel time and numerical first arrival of anisotropic waves is acceptable.

4.4 Numerical solution for the anisotropic Green's function in orthorhombic symmetry

The results of computing expression (82) applying a force in the origin and measuring waves in G_{11}, G_{22} and G_{33} for orthorhombic symmetry are here. The parameters of the medium are given in Table 9.

Parameters	**Values**
c_{11}	50.6 GPa
c_{33}	40.0 GPa
c_{55}	13.2 GPa
c_{23}	27.9 GPa
c_{12}	24.4 GPa
r_0	1300 m

Parameters	**Values**
c_{22}	46.2 GPa
c_{44}	11.0 GPa
c_{66}	15.6 GPa
c_{13}	21.5 GPa
ρ	2750 kg/m^3

Table 9: List of parameters for orthorhombic symmetry. The elastic constants are taken from Ikelle & Amundsen (2018).

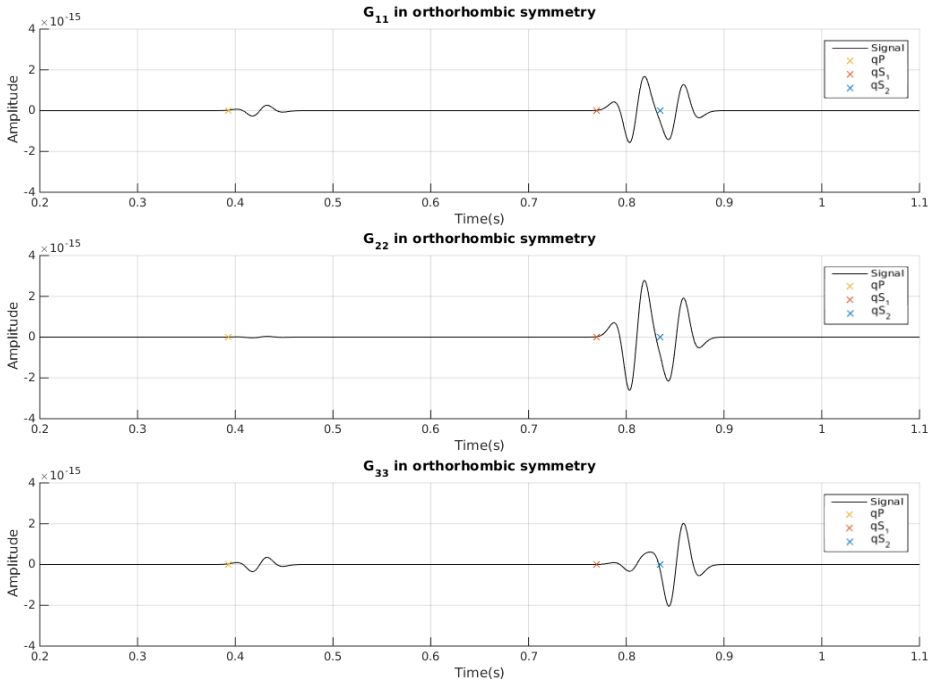

Figure 10: G_{11}, G_{22} and G_{33} solutions for orthorhombic symmetry. The color marks correspond to the travel time of the first arrival of the wavefields.

The comparison of analytical travel time and numerical first arrival of qP-, qS_1- and qS_2-waves are acceptable.

4.5 Numerical solution for the anisotropic Green's function in monoclinic symmetry

The seismograms obtained by applying a force in the origin and measuring waves in G_{11}, G_{22} and G_{33} for monoclinic symmetry are here. Parameters of the medium are given in Table 10.

Parameters	Values
c_{11}	35.8 GPa
c_{33}	24.0 GPa
c_{55}	7.80 GPa
c_{12}	14.4 GPa
c_{15}	2.50 GPa
c_{25}	3.80 GPa
c_{46}	0.38 GPa
r_0	1300 m

Parameters	Values
c_{22}	42.6 GPa
c_{44}	9.90 GPa
c_{66}	13.0 GPa
c_{13}	6.70 GPa
c_{23}	12.7 GPa
c_{35}	2.30 GPa
ρ	2216 kg/m^3

Table 10: List of parameters for monoclinic symmetry. The elastic constants are taken from Nevitt *et al.* (1988).

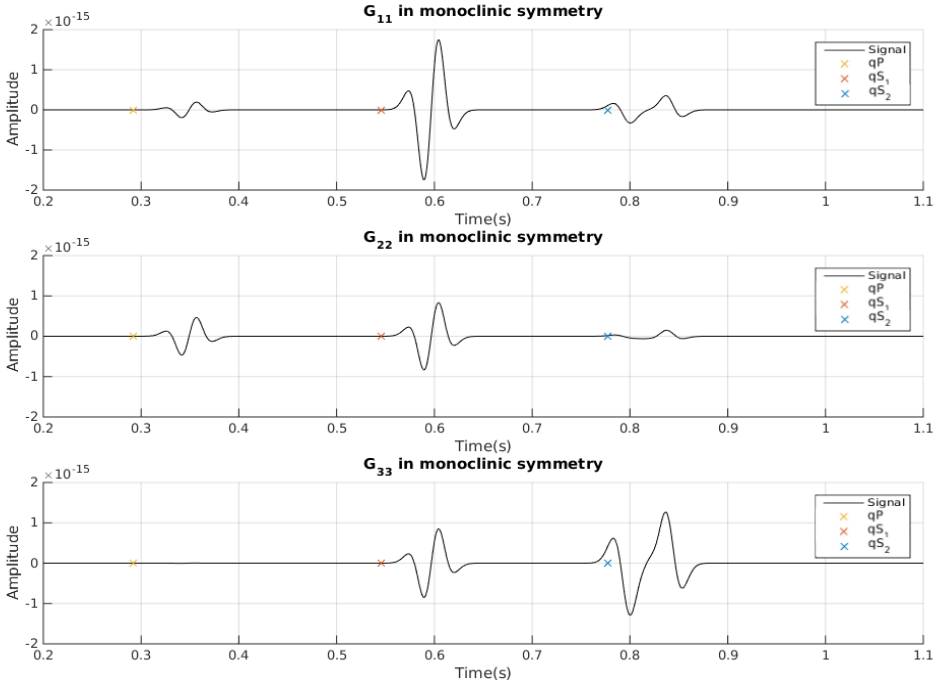

Figure 11: G_{11}, G_{22} and G_{33} solutions for monoclinic symmetry. The color marks correspond to the travel time of the first arrival of the wavefields.

4.6 Point-source radiation pattern: Transversely isotropic case

The radiation pattern in transversely isotropic symmetry for G_{11}, G_{22} and G_{33} is computed here. This experiment illustrates how the waveform changes with respect to polar angle. The wave amplitude is normalized to 1. For the study of qP-wave, a $\frac{\pi}{18}$ degree rotation is presented, and for qSV- and qSH-waves a $\frac{\pi}{8}$ rotation is used. The parameters of the medium are given in Table 5.

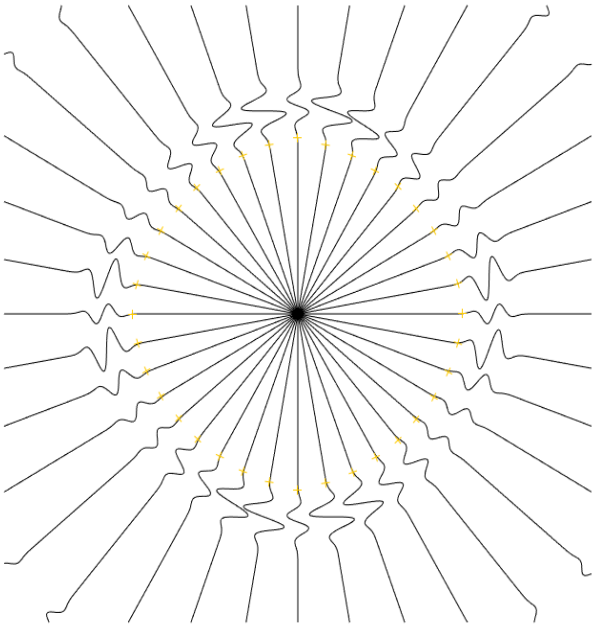

Figure 12: Radiation pattern of qP-wave in G_{11} component. The wave amplitude is normalized by 1. The color mark corresponds to the travel time of the first arrival of the wavefield.

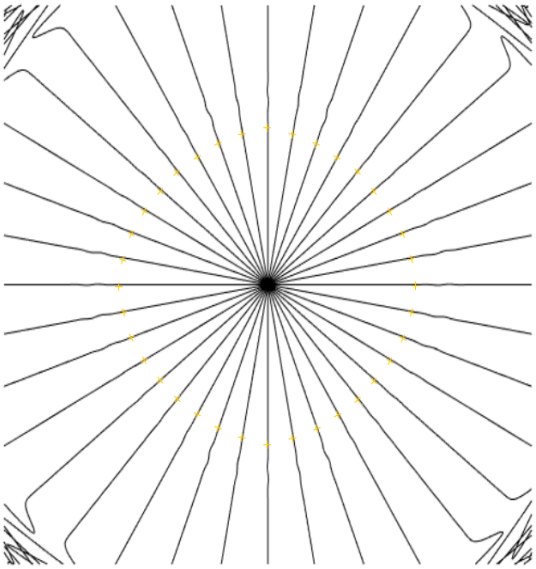

Figure 13: Radiation pattern of qP-wave in G_{22} component. The wave amplitude is normalized by 1. The color mark corresponds to the travel time of the first arrival of the wavefield.

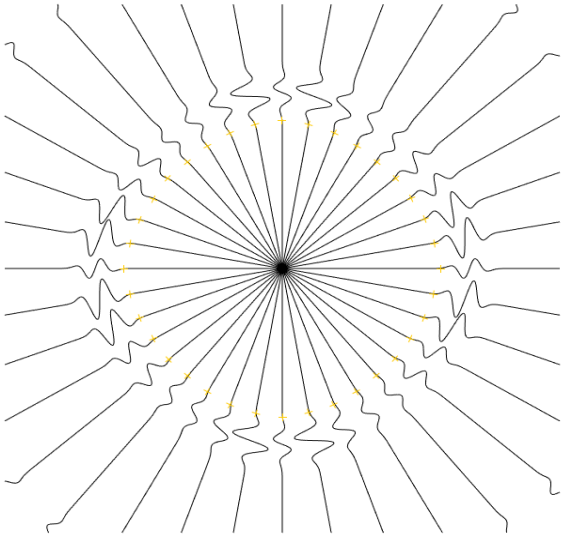

Figure 14: Radiation pattern of qP-wave in G_{33} component. The wave amplitude is normalized by 1. The color mark corresponds to the travel time of the first arrival of the wavefield.

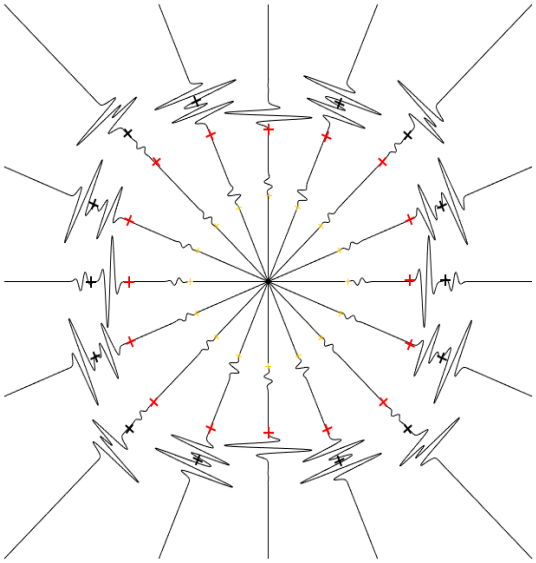

Figure 15: Radiation pattern of qSV- and qSH-waves in G_{11} component. The wave amplitude is normalized by 1. The color marks corresponds to the travel time of the first arrival of the wavefields.

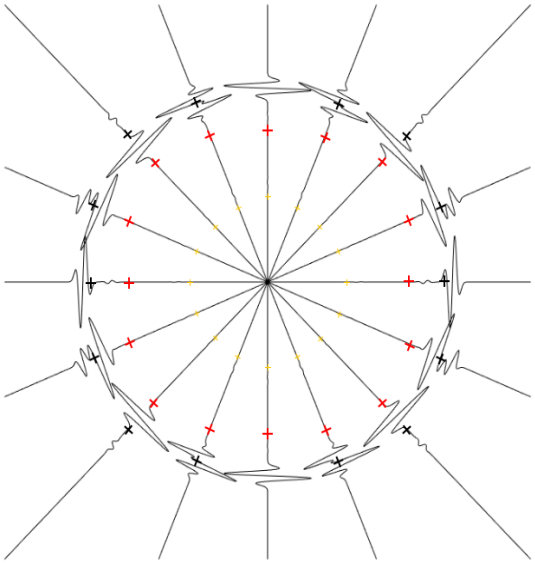

Figure 16: Radiation pattern of qSV- and qSH-waves in G_{22} component. The wave amplitude is normalized by 1. The color marks corresponds to the travel time of the first arrival of the wavefields.

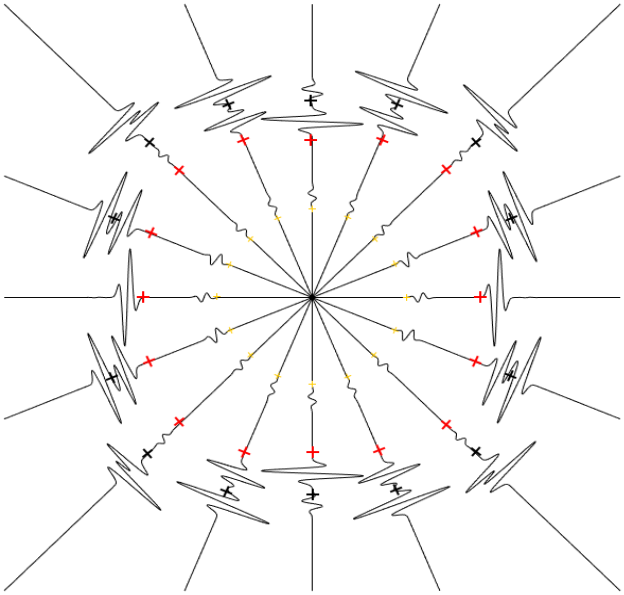

Figure 17: Radiation pattern of qSV- and qSH-waves in G_{33} component. The wave amplitude is normalized by 1. The color marks corresponds to the travel time of the first arrival of the wavefields.

From Figures 12, 13 and 14 we can observe the radiation pattern of qP-wave, by a point source applied in x_1 direction at the origin, in G_{11}, G_{22} and G_{33} components. In Figure 12 the qP-wave generated in G_{11} component shows the dependence of velocities on polar angle. The first arrival of qP-wave agrees with the numerical phase velocities(see Appendix A). From G_{22} component of Figure 13 we can observe how the qP-wave amplitude decreases compared with the other components. In G_{11} component from Figure 14 shows the same solution of G_{33} component from Figure 12 rotated by 90 degrees as it is expected for this kind of symmetry.

Figures 15, 16 and 17 show the radiation pattern in G_{11}, G_{22} and G_{33} components for the other two waves, qSV and qSH. In the three figures the change of the waveform, velocity and qSV- and qSH-waves decoupling in certain angle can be observed. In Figures 15 and 17 we can observe how the propagation direction affects the velocity of the qSV- and qSH-waves. The eigenvectors of the Kelvin-Christoffel matrix allow us to interpretation of which is the qSV- and qSH-waves. From G_{22} component plotted in Figure 16 we can observe how the qP-wave amplitude is smaller compared with the other component measurements.

Chapter 5 Concluding remarks and future work directions

Based on the presented work, the conclusions are as follows:

- The Radon transform is a simple and efficient alternative to obtain the anisotropic Green's function in elastodynamics because it avoids the complications found in the Fourier domain.
- The comparison of the analytical solution for the isotropic case with the numerical solution obtained in this work shows that the MatLab code to obtain the anisotropic Green's function works correctly.
- The numerical solutions generated in this work in TI and orthorhombic symmetries agree with the ones described in Helbig (1994).
- The study of TI symmetries by the radiation pattern helps to understand the nature of wave propagation from a different perspective.
- The understanding of the behaviors of the phenomena observed in anisotropic cases, i.e., the waveform and splitting of the S-wave, is useful.It can provide information about the orientation of the medium.

For future work, the extension of this program to obtain the Green's function for an anisotropic poroelastic model would be interesting. The poroelastic anisotropic model is an extended version of the elastic anisotropic model. The equations of both models have the same structure. The only difference is the size of some matrices, however, this doesn't change the functionality of the program.

Cited literature

Abramowitz, M. & Stegun, I. A. (1964). *Handbook of mathematical functions with formulas, graphs and mathematical tables*. Dover.

Auld, B. (1973). *Acoustic fields and waves in solids, Vol. 1.*. Wiley.

Ben-Menahem, A. & Sena, A. (1990). Seismic source theory in stratified anisotropic media. *Journal of Geophysical Research*, **95**.

Bhatia, A. & Singh, R, N. (1986). *Mechanics of deformable media*. Institute of Physics.

Buchwald, V. (1959). Elastic waves in anisotropic media. *Proceedings of the Royal Society*, **253**(1-4): 563–580.

Burridge, R. (1967). The singularity on the plane lids of the wave surface of elastic media with cubic symmetry. *The Quarterly Journal of Mechanics and Applied Mathematics*, **20**: 41–56.

Crampin, S. (1985). Evaluation of anisotropy by shear-wave splitting. *Geophysics*, **50**: 142–152.

Deans, S. (1983). *The Radon transform and some of its applications*. Wiley-Interscience.

Dong, W. & Schmitt, D. P. (1994). Simplified dynamic and static Green's functions in transversely isotropic media. *Geophysical Journal International*, **119**(1): 231–242.

Golub, G. & Van Loan, C. (1996). *Matrix computations*. The Johns Hopkins University Press.

Helbig, K. (1994). *Foundations of anisotropy for exploration seismics*, Vol. 22. Elsevier.

Helbig, K. (2003). The first 100 years of elastic anisotropy. *Journal of Applied Geophysics*, **54**: 163.

Hoffman, J. D. (1992). *Numerical methods for engineers and scientists*. McGraw-Hill, Inc.

Ikelle, L. T. & Amundsen, L. (2018). *Introduction to petroleum seismology*. SEG Books.

Kraut, E. A. (1963). Advances in the theory of anisotropic elastic wave propagation. *Review of Geophysics and Space Physics*, **1**: 401 – 448.

Musgrave, M. J. (1970). *Crystal acoustics*. Holden Day.

Nevitt, M., Chan, S.-K., Liu, J., Grimsditch, M., & Fang, Y. (1988). The elastic properties of monoclinic zro2. *Physica B+C*, **150**(1): 230 – 233.

Payton, R. G. (1983). *Elastic wave propagation in transversely isotropic media*. Springer.

Rudzki, M. (1898). Uber die gestalt elastischer wellen in gesteinen. *IV Studie aus der Theorie der Erdbebenwellen: Bulletin of the Academy of Sciences Cracow*, pp. 373–384.

Thomsen, L. (2002). *Understanding seismic anisotropy in exploration and exploitation*. SEG Books.

Tsvankin, I. (2013). *Seismic signatures and analysis of reflection data in anisotropic media, 3rd edition*. Elsevier.

Wang, C.-Y. & Achenbach, J. D. (1995). Three-dimensional time-harmonic elastodynamic Green's functions for anisotropic solids. *Proceedings of the Royal Society A: Mathematical, Physical and Engineering Sciences*, **449**(1937): 441–458.

Willis, J. (1980). Polarization approach to the scattering of elastic waves—I. Scattering by a single inclusion. *Journal of the Mechanics and Physics of Solids*, **28**: 287–305.

Zee Ma, Y. & Holditch, S. (2016). *Unconventional oil and gas resources handbook: evaluation and development*. Gulf Professional Publishing.

Appendix A Phase velocities in an arbitrary anisotropic medium

The phase velocity for any kind of anisotropy can be obtained in the wavenumber-frequency domain by decomposing the Kelvin-Christoffel matrix in terms of their eigenvalues and eigenvectors. Starting from equation (28)

$$\tilde{\mathscr{L}}_{ip} = c_{ijpq} k_j k_q - \delta_{ip} \rho \omega^2 = 0. \tag{94}$$

Introducing spherical coordinate system for the wavenumber vector $\mathbf{k}$, such that k_3 is align to the x_3 direction, and taking θ and ϕ as polar and azimuth angles, respectively,

$$\mathbf{k} = k\hat{\mathbf{i}}, \tag{95}$$

$$\hat{\mathbf{i}} = (\sin\phi\cos\theta, \sin\phi\sin\theta, \cos\phi)\,, \tag{96}$$

and the phase velocity denoted as

$$\frac{\omega}{k} \equiv v \tag{97}$$

equation (94) is

$$\mathbf{\Gamma} - \rho v^2 \mathbf{I} = \mathbf{0}, \tag{98}$$

where $\mathbf{I}$ is a 3×3 identity matrix and $\mathbf{\Gamma}$ is the Kelvin-Christoffel matrix,

$$\mathbf{\Gamma} = \begin{bmatrix} \Gamma_{11} & \Gamma_{12} & \Gamma_{13} \\ \Gamma_{12} & \Gamma_{22} & \Gamma_{23} \\ \Gamma_{13} & \Gamma_{23} & \Gamma_{33} \end{bmatrix}$$

where

$$\begin{aligned}
\Gamma_{11} &= c_{11}i_1^2 + c_{66}i_2^2 + c_{55}i_3^2 + 2c_{56}i_2i_3 + 2c_{15}i_1i_3 + 2c_{16}i_1i_2, \\
\Gamma_{22} &= c_{66}i_1^2 + c_{22}i_2^2 + c_{44}i_3^2 + 2c_{24}i_2i_3 + 2c_{46}i_1i_3 + 2c_{26}i_1i_2, \\
\Gamma_{33} &= c_{55}i_1^2 + c_{44}i_2^2 + c_{33}i_3^2 + 2c_{34}i_2i_3 + 2c_{35}i_1i_3 + 2c_{45}i_1i_2, \\
\Gamma_{12} &= c_{16}i_1^2 + c_{26}i_2^2 + c_{45}i_3^2 + (c_{25} + c_{46})\, i_2i_3 + (c_{14} + c_{56})\, i_1i_3 + (c_{12} + c_{66})\, i_1i_2, \\
\Gamma_{13} &= c_{15}i_1^2 + c_{46}i_2^2 + c_{35}i_3^2 + (c_{36} + c_{45})\, i_2i_3 + (c_{13} + c_{55})\, i_1i_3 + (c_{14} + c_{46})\, i_1i_2, \\
\Gamma_{23} &= c_{56}i_1^2 + c_{24}i_2^2 + c_{34}i_3^2 + (c_{23} + c_{44})\, i_2i_3 + (c_{36} + c_{45})\, i_1i_3 + (c_{25} + c_{46})\, i_1i_2.
\end{aligned}$$

The determinant of the Kelvin-Christoffel matrix(94) is a 3rd order polynomial in $\rho v^2 (\equiv X)$,

$$X^3 + a_2X^2 + a_1X + a_0 = 0 \tag{99}$$

where

$$a_2 = -(\Gamma_{11} + \Gamma_{22} + \Gamma_{33}), \tag{100}$$

$$a_1 = \Gamma_{11}\Gamma_{22} + \Gamma_{11}\Gamma_{33} + \Gamma_{22}\Gamma_{33} - \Gamma_{12}^2 - \Gamma_{13}^2 - \Gamma_{23}^2, \tag{101}$$

$$a_0 = \Gamma_{11}\Gamma_{23}^2 + \Gamma_{22}\Gamma_{13}^2 + \Gamma_{33}\Gamma_{12}^2 - \Gamma_{11}\Gamma_{22}\Gamma_{33} - 2\Gamma_{12}\Gamma_{13}\Gamma_{23}. \tag{102}$$

The algebraic manipulation has been carried out in Mathematica. The roots of this 3rd order polynomial are obtained by the companion matrix technique (Golub & Van Loan (1996), §7.4.6). This method solves for the roots of a polynomial by constructing a (companion) matrix with the characteristic equation that is the same as the polynomial in question. In this manner, solving for the characteristic equation is reduced to solving an eigenvalue problem. The companion matrix for this case is

$$C = \begin{bmatrix} 0 & 0 & -a_0 \\ 1 & 0 & -a_1 \\ 0 & 1 & -a_2 \end{bmatrix}. \tag{103}$$

The square root of the three roots obtained here divided by density (ρ) correspond to the three phase-velocities qP, qS_1 and qS_2.